Solving partial differential equations numerically on manifolds with arbitrary spatial topologies

Lee Lindblom *, Béla Szilágyi

Theoretical Astrophysics 350-17, California Institute of Technology, Pasadena, CA 91125, USA

ABSTRACT

A multi-cube method is developed for solving systems of elliptic and hyperbolic partial differential equations numerically on manifolds with arbitrary spatial topologies. It is shown that any three-dimensional manifold can be represented as a set of non-overlapping cubic regions, plus a set of maps to identify the faces of adjoining regions. The differential structure on these manifolds is fixed by specifying a smooth reference metric tensor. Matching conditions that ensure the appropriate levels of continuity and differentiability across region boundaries are developed for arbitrary tensor fields. Standard numerical methods are then used to solve the equations with the appropriate boundary conditions, which are determined from these inter-region matching conditions. Numerical examples are presented which use pseudo-spectral methods to solve simple elliptic equations on multi-cube representations of manifolds with the topologies T^3, $S^2 \times S^1$ and S^3. Examples are also presented of numerical solutions of simple hyperbolic equations on multi-cube manifolds with the topologies $R \times T^3$, $R \times S^2 \times S^1$ and $R \times S^3$.

© 2013 Elsevier Inc. All rights reserved.

1. Introduction

The need to solve partial differential equations on manifolds having non-trivial spatial topologies arises in many areas of physical science: from models of wormholes or the global structure of the universe in general relativity theory to global circulation models of the earth's atmosphere in meteorology and climatology. This paper develops practical methods for solving a variety of partial differential equations on manifolds having arbitrary spatial topologies. Every n-dimensional manifold (by definition) can be mapped locally into a portion of n-dimensional Euclidean space, R^n. A number of different numerical methods are capable of solving partial differential equations locally on open subsets of R^n. The topological structure of a manifold, however, affects the global solutions to partial differential equations in profound ways. This paper develops methods for fitting together local solutions, obtained from standard numerical methods, to form the desired global solutions on manifolds with arbitrary topologies. The discussion here focuses on solving elliptic systems of equations on three-dimensional manifolds Σ with arbitrary topologies, and also hyperbolic systems of equations on four-dimensional manifolds with topologies $R \times \Sigma$.

Solving partial differential equations numerically on manifolds with arbitrary topologies requires the creation of computational infrastructures (beyond those needed to solve the equations numerically on open subsets of R^n) that meet two basic requirements. The first requirement is that the manifold must be represented in a way that allows the points in the manifold, and the values of scalar and tensor fields defined at those points, to be referenced efficiently in a way that respects the underlying topological structure of the manifold. The second requirement is to create a way to specify the global differential

---

* Corresponding author. Tel.: +1 626 395 4911.
E-mail address: lindblom@tapir.caltech.edu (L. Lindblom).

structure of the manifold, i.e. the computational method must provide a way of representing globally continuous and differentiable scalar and tensor fields on these manifolds. The goal here is to develop practical methods that can be used on arbitrary manifolds by a wide range of different numerical methods.

The first requirement is to find a systematic way of representing manifolds with arbitrary topologies. Every n-dimensional manifold can be mapped locally into a portion of n-dimensional Euclidean space R^n. For computational efficiency (and to avoid certain types of numerical instabilities) each manifold is represented here by a collection of non-overlapping n-dimensional cubes which cover the manifold, plus a set of maps that identify the faces of adjoining n-cubes. This decomposition is analogous to representing a manifold as a collection of non-intersecting n-simplexes (i.e. triangles for $n = 2$ and tetrahedrons for $n = 3$) that cover the manifold, plus maps that identify neighboring faces. Many numerical methods (including the pseudo-spectral methods used to produce illustrative examples for this paper) are easier to use in computational domains based on n-cubes rather than n-simplexes. Points in each of the n-cube regions are identified by local Cartesian coordinates, and these coordinates are used to represent the solutions to the differential equations in each n-cube. This type of representation has been used for some time in numerical methods for solving partial differential equations on a two-sphere [1–3], and also in three-dimensional manifolds that are subsets of R^3 [4–10]. Those ideas are generalized in Section 2, and it is shown that these generalizations can be applied to two-dimensional or three-dimensional manifolds having arbitrary topologies. Examples of these multi-cube representations are given in Appendix A for the three-dimensional manifolds with the topologies T^3, $S^2 \times S^1$, and S^3.

The second requirement is to develop a method of representing (at least in the continuum limit) continuous and differentiable tensor fields on the multi-cube representations of manifolds developed in Section 2. Representing tensor fields within each of the n-cube regions is straightforward: their components can be expressed in the tensor bases associated with the local Cartesian coordinates. These tensor components are functions of those coordinates, and their continuity (or differentiability) determines the continuity (or differentiability) of the tensor field itself. In general, however, the coordinate tensor bases associated with different n-cube regions are not even continuous (and cannot be made continuous globally) across the interfaces that join them. The problem of defining the continuity and differentiability of tensor fields across n-cube interfaces is therefore non-trivial. The method introduced here makes use of a smooth reference metric tensor. This reference metric must be supplied (along with the collection of n-cube regions and the associated interface maps) as part of the specification of a particular manifold. This metric is used to construct geometrical normal vectors at each interface, and these normals are used to construct the Jacobian matrices that map vectors (and tensors) across interfaces. The differentiability of tensors across the n-cube interfaces is defined in terms of the continuity of the covariant derivatives of those tensors, using the covariant derivative associated with the reference metric. The details of these continuity and differentiability conditions are given in Section 3. Examples of reference metrics which can be used to implement these continuity and differentiability conditions are given in Appendix A for the three-dimensional manifolds with the topologies T^3, $S^2 \times S^1$, and S^3.

Systems of differential equations can be solved numerically on multi-cube representations of manifolds by fitting together local solutions from each n-cube region. The appropriate local solutions are determined in each region by applying the correct boundary conditions on the n-cube faces. The appropriate boundary conditions are the ones that enforce the needed level of continuity and differentiability of the global solution at the region boundaries. These boundary conditions are developed in Section 4 for second-order strongly elliptic systems, and also for first-order symmetric hyperbolic systems of equations. These boundary conditions select the unique local solution in a particular n-cube that equals the desired global solution in that region. The collection of local solutions to the equations constructed in this way provides the desired global solution.

The multi-cube method of solving systems of partial differential equations numerically on manifolds with non-trivial topologies is illustrated here by solving a series of test problems in Sections 5 and 6. Simple second-order elliptic equations, and first-order symmetric hyperbolic equations, are solved numerically on manifolds with spatial topologies T^3, $S^2 \times S^1$, and S^3. These tests use pseudo-spectral methods to produce local solutions on each cubic region. The results are shown to converge exponentially (in an L^2 norm) to the exact global solutions (which are known analytically for these test problems) as the number of grid points used for the solution is increased.

2. Building multi-cube manifolds

This section describes how n-dimensional manifolds can be represented using the multi-cube method. The idea is quite simple: n-dimensional multi-cube representations of manifolds consist of a set of non-overlapping n-cubes that cover the manifold, plus a set of maps that identify the boundary faces of neighboring cubes. An argument is presented in Section 2.1 that all two-dimensional and all three-dimensional manifolds (with arbitrary topologies) can be represented in this way. A large class (but not all) higher-dimensional manifolds can also be represented using this multi-cube method. The multi-cube method provides a way of representing manifolds that facilitates the design of computational tools for solving partial differential equations on them. A simple infrastructure is introduced in Section 2.2 for systematically building, referencing and identifying the faces of the needed sets of n-cubes in these manifolds. These n-cube regions are joined together to form the desired topological manifold using maps that identify points on the faces of neighboring n-cubes. A simple framework for building and referencing these maps is presented. Only a small number of topologically distinct maps are needed for the case of three-dimensional manifolds (the main focus of this paper), and all of those maps are given explicitly.

2.1. Existence of multi-cube representations

This subsection considers the question of whether two- and three-dimensional manifolds with arbitrary topologies admit multi-cube representations. The first step is to show that every two-manifold is homeomorphic to a set of squares (i.e. 2-cubes) glued together along their edges. The proof is based on the result of Radó [11] (see also Moise [12]) that all two-dimensional manifolds admit triangulations, i.e. that any two-manifold is homeomorphic to a set of triangles glued together along their edges. It is easy to show that a simple refinement of any triangulation on a two-dimensional manifold produces a multi-cube representation of that manifold. As illustrated in Fig. 1, let points "A", "B", and "C" denote the vertexes of one of the triangles in the triangulation. Add the midpoints of each edge of this triangle as additional vertexes, labeled "ab", "bc", and "ac" in Fig. 1. Next, add the centroid of the triangle, the point labeled "d", and finally add as additional edges the line segments that connect "d" with the midpoints "ab", "bc" and "ac". The resulting complex consists of three quadrilaterals. When all of the triangles in a given triangulation are refined in this way, the result is a multi-cube representation of the two-manifold. The refinement consists of a set of quadrilaterals that are glued together edge to edge. Since the additional edge vertexes, "ab", etc. are always added at the geometrical midpoints, the edges of neighboring quadrilaterals constructed in this way will always coincide. These quadrilaterals are homeomorphic to squares (2-cubes). So the topological structure of a two-manifold can be thought of as a collection of non-overlapping 2-cubes that cover the manifold, plus a set of maps that identify the edges of adjoining 2-cubes.

A similar argument shows that every three-dimensional manifold has a multi-cube representation, i.e. that every three-dimensional manifold is homeomorphic to a set of non-overlapping "distorted" cubes glued together at their faces. The proof is based on a result of Moise [12,13] that all three-dimensional manifolds admit triangulations by tetrahedrons, i.e. that any three-dimensional manifold is homeomorphic to a set of non-overlapping tetrahedrons glued together at their faces. It is easy to show that any tetrahedron can be decomposed into four "distorted" cubes glued together at their faces (the term distorted cube is used here to describe a solid having six faces, each of which is a plane quadrilateral). Distorted cubes are homeomorphic to geometrical cubes. It follows that every triangulation of a three-manifold can be refined (by adding appropriate vertexes, edges and faces) to obtain a multi-cube representation, i.e. a set of non-overlapping distorted cubes glued together at their faces. This argument demonstrates the existence of multi-cube representations for any three-dimensional manifold.

The key to this argument is the representation of a single tetrahedron as four distorted cubes glued together. This can be done by refining the tetrahedron through the addition of vertexes, edges and faces as summarized in Fig. 2. Begin with a tetrahedron with vertexes labeled "A", "B", "C" and "D". First add vertexes to the midpoints of each edge, plus vertexes to the centroids of each face, the points "a", "b", "c" and "d" shown in the top left of Fig. 2. Adding the extra edges connecting "a", "b", "c" and "d" to the midpoints of each edge of the original tetrahedron completes the decomposition of each face into a set of distorted squares. Add one last vertex at the centroid of the tetrahedron, labeled "O" in the top right of Fig. 2. Connect "O" to the facial centroids, "a", "b", "c" and "d", by adding the edges shown as dash-dot line segments in the top right of Fig. 2. Finally add the six internal quadrilateral faces that include the point "O" as an edge vertex. These additional vertexes, edges, and faces divide the tetrahedron into four volume regions (one adjacent to each tetrahedron vertex). The bottom of Fig. 2 shows these four regions more clearly. The regions adjacent to the vertexes "A" and "C" are shown with opaque faces, while those adjacent to "B" and "D" are shown with transparent faces.

Each of the four volume regions constructed above has six faces, and each of these faces has four edges and four vertexes. These faces are therefore quadrilaterals. It only remains to show that these quadrilaterals are planar. Call two edges of the original tetrahedron "complimentary" if they do not intersect at a vertex, e.g. the edges "AC" and "BD" are complimentary. Now consider the six bisecting planes of the tetrahedron, each one formed by an edge and the midpoint of the complementary edge of the tetrahedron. Each bisecting plane passes through the midpoint of the complementary edge, the centroid "O", as well as the facial centroids of the two faces adjacent to the complementary edge. For example, the bisecting plane formed by the edge "AC" and midpoint "bd" intersects "O" as well as the facial centroids "a" and "c". The quadrilateral formed by the vertexes "bd", "a", "O", and "c" is therefore a planar quadrilateral. It follows that each of the faces of the four volume regions is a planar quadrilateral, and therefore each volume region is a distorted cube.
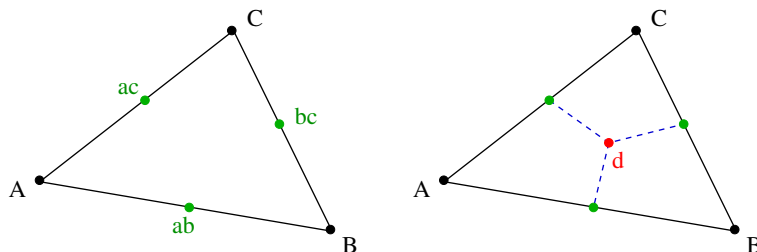
Fig. 1. Each triangle in a triangulation of a two-dimensional manifold is refined by the addition of extra vertexes and edges to produce three quadrilaterals. This is done by first adding as new vertexes the midpoints of each edge, i.e. the points "ab", "bc" and "ac" in the figure on the left. Next the centroid of the triangle, i.e. the point "d" in the figure on the right, is also added as a new vertex. Finally the line segments that join "d" to the midpoints "ab", "bc", and "ac", the dashed lines in the figure on the right, are added as new edges.
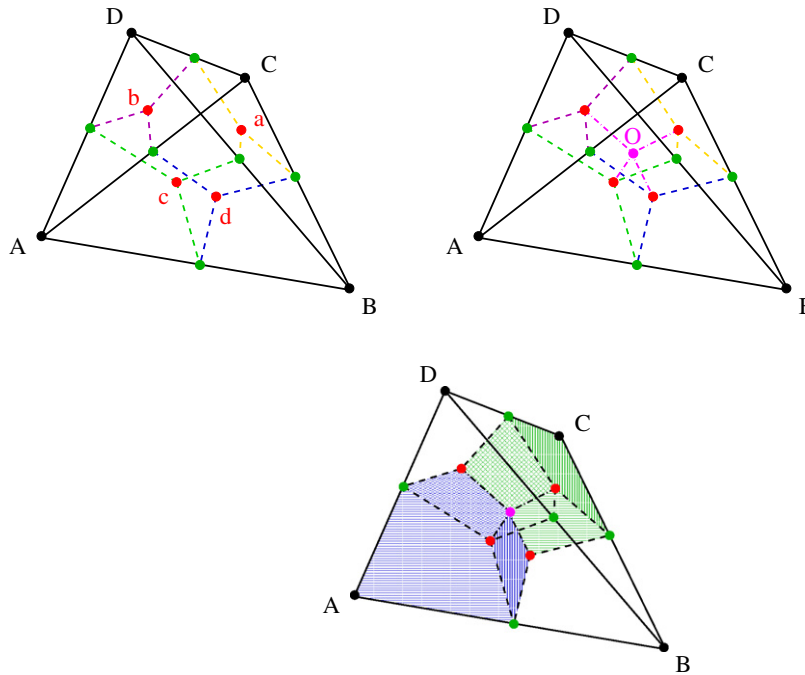
Fig. 2. Top Left: Label the vertexes of the tetrahedron "A", "B", "C" and "D". Add vertexes at the midpoints of each edge, and additional vertexes at the centroid of each face of the tetrahedron, labeled "a" for the centroid of face "BCD", "b" for face "ACD", etc. Also add additional edges (shown as dashed line segments) connecting each centroid to the midpoint of each adjoining edge. Top Right: Add one additional vertex, labeled "O" at the centroid of the tetrahedron. Add additional edges (shown as dash-dot line segments) that connect "O" to the centroids of each face, and six additional faces that include "O" as a vertex. Bottom: Four "distorted" cubes that make up the tetrahedron are illustrated. The two cubes adjacent to vertexes "A" and "C" are shown with opaque shaded faces, while the faces of the cubes adjacent to "B" and "D" are transparent.

The vertexes added in this construction were placed at the geometric centroids of the triangular faces, and at the centroid of the original tetrahedron. The edges added in this construction were also placed in geometrically determined ways: all of them along one of the bisecting planes of each edge of the original tetrahedron. These geometrically constructed features will therefore match on the triangular boundaries between neighboring tetrahedrons in any triangulation of a three-dimensional manifold. It follows that the distorted cubes constructed in this way will match face-to-face across all the tetrahedron boundaries as required for a multi-cube representation of the manifold.

2.2. Infrastructure for multi-cube manifolds

Now turn to the problem of finding a systematic way of constructing multi-cube manifolds. The goal is to develop methods that can be used as part of the computational infrastructure for solving systems of partial differential equations on such manifolds. The discussion here is focused on three-dimensional manifolds Σ, but generalizations to other dimensions should be fairly straightforward. Let $\mathcal{B}_A$ denote a collection of geometrical cubic regions in R^3. The subscript $A = \{1, \ldots, N\}$ is used to label the individual regions.[1] These cubes are used here as the domains of coordinate charts for the multi-cube representation of Σ. Let Ψ_A denote the invertible coordinate map that takes the region $\mathcal{B}_A$ into a subset of Σ: $\Psi_A(\mathcal{B}_A) \subset \Sigma$. It will be useful to denote the boundary faces of these regions in R^3 as $\partial_\alpha \mathcal{B}_A$, where $\alpha = \pm x$ denotes the faces intersecting the $\pm x$ axes, $\alpha = \pm y$ the faces intersecting the $\pm y$ axes, etc.

The discussion above shows that every three-manifold can be covered by a collection of non-overlapping cubes: $\cup_A \Psi_A(\mathcal{B}_A) = \Sigma$. Non-overlapping here means that the images of the regions are non-intersecting, $\Psi_A(\mathcal{B}_A) \cap \Psi_B(\mathcal{B}_B) = \emptyset$, for points in the interiors of $\mathcal{B}_A$ and $\mathcal{B}_B$ when $A \neq B$. It is convenient to choose the regions $\mathcal{B}_A$ in R^3 to be scaled so they all have the same size L, and are all oriented along the same global Cartesian coordinate axes in R^3. In this case the region $\mathcal{B}_A$ is completely determined therefore simply by specifying the location of its center $\vec{c}_A = (c_A^x, c_A^y, c_A^z)$ in R^3. It is also convenient to arrange the regions $\mathcal{B}_A$ in R^3 so they intersect (if at all) in R^3 only at points on faces whose images also intersect in Σ. In the multi-cube representations of manifolds satisfying these conditions, each point in the interior of the regions represents a unique point in Σ, and each point in Σ is the image of at least one point in the closure of $\cup_A \mathcal{B}_A$. The Cartesian coordinates

---

[1] The term region in this paper is used to refer to the cubes $\mathcal{B}_A$ that form the basic topological structure of the manifold. It might be useful for computational efficiency to subdivide some (or all) of the cubic regions into a collection of smaller cubes, e.g. by cutting a cubic region into two, four, or eight smaller cubes. Those smaller cubic subsets of the $\mathcal{B}_A$ are referred to as subregions.

of R^3 therefore provide a global way of identifying points in Σ. Tensor fields are represented on these multi-cube manifolds by giving the values of their components (expressed in the coordinate basis of R^3) as functions of these global Cartesian coordinates.

A multi-cube manifold consists of a set of cubic regions, $\mathcal{B}_A$ for $A = \{1, \ldots, N\}$ that can be specified simply by giving the locations of their centers $\vec{c}_A$, along with a set of rules that determine how the faces of these cubes are to be identified with one another. When points on the images of two boundary faces $\Psi_A(\partial_\alpha \mathcal{B}_A)$ and $\Psi_B(\partial_\beta \mathcal{B}_B)$ intersect in Σ, then the associated coordinate charts provide an invertible map from one boundary face to the other: $\partial_\alpha \mathcal{B}_A = \Psi_{B\beta}^{A\alpha}(\partial_\beta \mathcal{B}_B)$ where $\Psi_{B\beta}^{A\alpha} \equiv \Psi_A^{-1} \circ \Psi_B$ for points on the $\partial_\alpha \mathcal{B}_A$ and $\partial_\beta \mathcal{B}_B$ faces. Since the cubes $\mathcal{B}_A$ have uniform size and orientation in R^3, there are only a small number of simple maps $\Psi_{B\beta}^{A\alpha}$ needed to represent all the topologically distinct ways of mapping one face onto another. It is sufficient to consider maps that identify the faces of two cubic region first by rigidly translating so the centers of the faces $\partial_\alpha \mathcal{B}_A$ and $\partial_\beta \mathcal{B}_B$ coincide, and then rigidly rotating and/or reflecting to align the two faces in the desired way. Thus it is sufficient to consider the simple maps $\Psi_{B\beta}^{A\alpha}$ that take the Cartesian coordinates x_B^i of points in $\partial_\beta \mathcal{B}_B$ to the Cartesian coordinates x_A^i of the corresponding points in $\partial_\alpha \mathcal{B}_A$ in the following way,

$$x_A^i = c_A^i + f_\alpha^i + C_{B\beta j}^{A\alpha i}\left(x_B^j - c_B^j - f_\beta^j\right). \tag{1}$$

The vector $\vec{c}_A + \vec{f}_\alpha$ is the location of the center of the $\partial_\alpha \mathcal{B}_A$ face, and $\mathbf{C}_{B\beta}^{A\alpha}$ is the combined rotation and reflection matrix needed to achieve the desired orientation. Examples of the use of these methods is given in Appendix A where explicit multi-cube representations are constructed for manifolds with the topologies T^3, $S^2 \times S^1$ and S^3.

Multi-cube manifolds are specified by giving the list of cubic regions $\mathcal{B}_A$ needed to cover the manifold, the vectors $\vec{c}_A$ that determine the locations of their centers in R^3, and the maps $\Psi_{B\beta}^{A\alpha}$ that determine how the regions are glued together. These maps, defined in Eq. (1), depend on the vectors $\vec{c}_A$ and $\vec{f}_\alpha$, and the matrix $\mathbf{C}_{B\beta}^{A\alpha}$, so these quantities must all be specified to determine each map. The vector $\vec{f}_\alpha$ is the position of the center of the α face relative to the center of the region. Since the cubic regions are chosen to have uniform sizes and orientations, $\vec{f}_\alpha$ has the same form in each cubic region:

$$\begin{aligned}
\vec{f}_{\pm x} &= \tfrac{1}{2}L(\pm 1, 0, 0), \\
\vec{f}_{\pm y} &= \tfrac{1}{2}L(0, \pm 1, 0), \\
\vec{f}_{\pm z} &= \tfrac{1}{2}L(0, 0, \pm 1),
\end{aligned} \tag{2}$$

where L is the size of the cubes. Since all of the cubic regions are aligned, the class of possible rotations and reflections needed for $\mathbf{C}_{B\beta}^{A\alpha}$ is quite small. These can all be constructed by combining 90-degree rotations about the normal to one of the faces, $\mathbf{R}_\alpha$, with mirror reflections about some (possibly different) direction, $\mathbf{M}_\beta$. Table 1 gives explicit expressions for the matrices that describe these elementary rotations and reflections in three dimensions. The most general transformation of one face onto another can be constructed by taking products of these elementary transformations. The group of possible $\mathbf{C}_{B\beta}^{A\alpha}$ in three dimensions generated in this way is therefore the octahedral symmetry group, O_h, which has 48 distinct elements [14]. The orientation preserving subgroup generated by the rotations alone has 24 elements. Note that $\mathbf{R}_\alpha \cdot \mathbf{R}_{-\alpha} = \mathbf{R}_\alpha^4 = \mathbf{M}_\alpha^2 = \mathbf{I}$, where $\mathbf{I}$ is the identity matrix. Since the number of possible maps $\Psi_{B\beta}^{A\alpha}$ constructed in this way is so small, it is easy to write a flexible code that is capable of setting up the multi-cube structures and all the needed gluing maps for three-manifolds with arbitrary topologies.

3. Specifying differential structures on multi-cube manifolds

This section describes a practical and efficient way to define C^k differential structures on multi-cube manifolds. It is useful to begin with a brief discussion of the traditional way such structures are defined. The differential structure on a manifold provides the framework needed to represent differentiable scalar and tensor fields on that manifold. The usual method of specifying a differential structure is to cover the manifold with a set of overlapping domains $\mathcal{D}_A$, and set of maps Υ_A that assign coordinates to the points in each domain: $\Upsilon_A^{-1}(\mathcal{D}_A) \subset R^n$. These coordinate maps provide a differential structure for the manifold if they have the property that the composition maps $\Upsilon_B^A = \Upsilon_A^{-1} \circ \Upsilon_B$ are differentiable (or C^{k+1}) transformations from the coordinates of one patch to the other for points in the overlap $\mathcal{D}_A \cap \mathcal{D}_B$. The Jacobian matrices associated with these

Table 1
Elementary Transformations.

	$\alpha = \pm x$	$\alpha = \pm y$	$\alpha = \pm z$
$\mathbf{R}_\alpha$	$\begin{pmatrix} 1 & 0 & 0 \\ 0 & 0 & \mp 1 \\ 0 & \pm 1 & 0 \end{pmatrix}$	$\begin{pmatrix} 0 & 0 & \pm 1 \\ 0 & 1 & 0 \\ \mp 1 & 0 & 0 \end{pmatrix}$	$\begin{pmatrix} 0 & \mp 1 & 0 \\ \pm 1 & 0 & 0 \\ 0 & 0 & 1 \end{pmatrix}$
$\mathbf{M}_\alpha$	$\begin{pmatrix} -1 & 0 & 0 \\ 0 & 1 & 0 \\ 0 & 0 & 1 \end{pmatrix}$	$\begin{pmatrix} 1 & 0 & 0 \\ 0 & -1 & 0 \\ 0 & 0 & 1 \end{pmatrix}$	$\begin{pmatrix} 1 & 0 & 0 \\ 0 & 1 & 0 \\ 0 & 0 & -1 \end{pmatrix}$

coordinate transformations $J_{Bj}^{Ai} = \partial x_A^i/\partial x_B^j$ determine the transformations for C^k differentiable tensors from one coordinate representation to another in these overlaps.

It is possible to use the traditional method of defining differential structures on multi-cube manifolds, but to do so requires that non-trivial additional structures must be added to the basic multi-cube construction (since the domains that define that basic structure do not overlap). The most straightforward approach would be to require that each multi-cube manifold be provided with an additional set of overlapping domains $\mathcal{D}_A \supset \Psi_A(\mathcal{B}_A)$ and a set of C^{k+1} related coordinate maps Υ_A for the new overlapping $\mathcal{D}_A$ domains. An alternative, more minimalist, approach would be to require that suitable Jacobian matrices $J_{B\beta j}^{A\alpha i}$, in addition to the connection maps $\Psi_{B\beta}^{A\alpha}$, be provided on each interface between regions in multi-cube manifolds. This minimal structure would provide the transformations needed to define differentiable scalar and continuous tensor fields on these manifolds. If C^{k+1} differentiable scalars or C^k differentiable tensor fields are needed, then in addition to $J_{B\beta j}^{A\alpha i}$, all of their kth order derivatives $\partial_B^k J_{Bj}^{Ai}$ would also have to be specified on each interface between regions.

It might seem redundant and unnecessary to require that the Jacobian matrices $J_{B\beta j}^{A\alpha i}$ and their derivatives be specified on the interfaces in multi-cube manifolds, in addition to the interface coordinate maps $\Psi_{B\beta}^{A\alpha}$ defined in Eq. (1). After all, the Jacobian matrices associated with those interface maps, $J_{B\beta j}^{A\alpha i} = C_{B\beta j}^{A\alpha i}$, and their derivatives, $\partial_{Bk} J_{B\beta j}^{A\alpha i} = \partial_{Bk} C_{B\beta j}^{A\alpha i} = 0$, could be used to transform tensor fields at the boundary interfaces. Unfortunately it is easy to see that the coordinate maps Ψ_A used in Section 2 to construct the multi-cubes are not suitable for constructing a global C^k differential structure on most manifolds. If they were, the basis vectors ∂_{Ai} associated with these coordinates would be smooth global non-vanishing vector fields. These vector fields could be used in this case to construct a global smooth flat metric on the manifold. Since most manifolds do not admit global flat metrics, the existence of a complete set of smooth non-vanishing coordinate vector fields cannot exist on most manifolds. Fig. 3, drawn from the perspective of a smooth coordinate patch that covers both sides of an interface boundary, illustrates how the multi-cube coordinates in neighboring regions can be continuous while failing to be differentiable across region boundaries. The coordinate region $\mathcal{B}_1$ on the left, matches to coordinate region $\mathcal{B}_2$ on the right across the $X_1 = X_2$ interface in Fig. 3. The coordinate vectors tangent to this interface, e.g. ∂_{Y_1} and ∂_{Y_2}, are continuous across this interface, while those not tangent to the boundary, i.e. ∂_{X_1} and ∂_{X_2}, are discontinuous there.

Both approaches described above for specifying differential structures on a multi-cube manifolds require that a great deal of extra structure be provided. This paper proposes a third, more elegant and more efficient, approach that can be incorporated more easily into the computational infrastructure for solving partial differential equations numerically. Every manifold with a C^{k+1} differential structure admits a symmetric positive definite C^k differentiable metric tensor g_{ij}. The method proposed here for specifying the global differential structure on a multi-cube manifold requires that the components of (any) one of these C^k differentiable reference metrics, g_{ij}, be provided in the global Cartesian coordinate basis used to define the multi-cube manifold. The components of this reference metric g_{ij} will be C^k functions of the multi-cube Cartesian coordinates within each region $\mathcal{B}_A$, but will (in general) be discontinuous across the interfaces between regions. The only requirement on this reference metric is that it must be sufficiently smooth, C^k, when represented in a global C^{k+1} coordinate atlas. The C^{k+1} coordinate charts Υ_A themselves need not be given as part of the specification of the multi-cube manifold. Their only use in this method is to ensure *a priori* that the reference metric meets the needed smoothness requirements.

Once a suitable reference metric g_{ij} is provided, it is straightforward to construct the Jacobian matrices $J_{B\beta j}^{A\alpha i}$ and the dual Jacobian matrices $J_{A\alpha i}^{*B\beta j}$ needed to transform continuous tensor fields across the interface boundaries in multi-cube manifolds. Assume that the $\partial_\alpha \mathcal{B}_A$ boundary of region $\mathcal{B}_A$ is identified with the $\partial_\beta \mathcal{B}_B$ boundary of region $\mathcal{B}_B$ by the map $\Psi_{B\beta}^{A\alpha}$ given in Eq. (1). The transformation taking the region $\mathcal{B}_B$ representation of a vector v_B^i into the region $\mathcal{B}_A$ representation v_A^i at one of these identified boundary points is an expression of the form

$$v_A^i = J_{B\beta j}^{A\alpha i} v_B^j, \tag{3}$$

where $J_{B\beta j}^{A\alpha i}$ is in effect the Jacobian matrix of the transformation. The analogous transformation law for covectors w_{Bi} is,

$$w_{Ai} = J_{A\alpha i}^{*B\beta j} w_{Bj}, \tag{4}$$

where $J_{A\alpha i}^{*B\beta j}$ is in effect the dual Jacobian matrix.
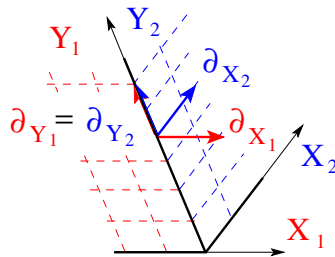
Fig. 3. Maps Ψ_A define continuous but (typically) non-differentiable transitions between cubic regions. This example shows that the basis vectors tangent to the boundary, ∂_{Y_1} and ∂_{Y_2}, are continuous, while those not tangent to the boundary, ∂_{X_1} and ∂_{X_2}, are not.

Let g_{Aij} denote the coordinate components of the reference metric in the multi-cube coordinate basis of region $\mathcal{B}_A$, and let $n_{A\alpha i}$ denote the outward directed normal covector to the surface $\partial_\alpha \mathcal{B}_A$. This interface is a surface of constant coordinate x_A^α, so the geometrical normal covector is proportional to $\partial_{Ai} x_A^\alpha$. The normal covector is therefore given by

$$n_{A\alpha i} = \frac{\pm \partial_{Ai} x_A^\alpha}{\sqrt{g_A^{jk} \partial_{Aj} x_A^\alpha \partial_{Ak} x_A^\alpha}}, \tag{5}$$

where g_A^{ij} is the inverse of the reference metric g_{Aij}. The sign is chosen in this expression to make $n_{A\alpha i}$ the outgoing unit normal. The unit normal vector $n_{A\alpha}^i$ is related to $n_{A\alpha i}$ by $n_{A\alpha}^i = g_A^{ij} n_{A\alpha j}$.

The Jacobian matrices needed to transform vectors and covectors (and therefore any type of tensor field) across boundary interfaces are simple functions of the quantities $C_{B\beta j}^{A\alpha i}$ and $C_{A\alpha i}^{B\beta j}$ (which define the identification maps $\Psi_{B\beta}^{A\alpha}$), as well as the normals to the boundary surface, $n_{A\alpha}^i$, $n_{A\alpha i}$, $n_{B\beta}^i$ and $n_{B\beta i}$:

$$J_{B\beta j}^{A\alpha i} = C_{B\beta k}^{A\alpha i} \left(\delta_j^k - n_{B\beta}^k n_{B\beta j} \right) - n_{A\alpha}^i n_{B\beta j}, \tag{6}$$

$$J_{A\alpha i}^{*B\beta j} = \left(\delta_i^k - n_{A\alpha i} n_{A\alpha}^k \right) C_{A\alpha k}^{B\beta j} - n_{A\alpha i} n_{B\beta}^j. \tag{7}$$

The Jacobian matrices defined in Eqs. (6) and (7) are the unique ones with the properties: (a) They map the geometrical normals $n_{B\beta}^j$ into $-n_{A\alpha}^i$ and $n_{B\beta j}$ into $-n_{A\alpha i}$,

$$n_{A\alpha}^i = -J_{B\beta j}^{A\alpha i} n_{B\beta}^j, \tag{8}$$

$$n_{A\alpha i} = -J_{A\alpha i}^{*B\beta j} n_{B\beta j}, \tag{9}$$

(i.e. the outward directed normal of one region is identified with the inward directed normal of its neighbor). (b) The Jacobian matrix $J_{B\beta j}^{A\alpha i}$ transforms any vector t^i tangent to the boundary (i.e. any vector satisfying $t^i n_i = 0$) using the continuity of the $\Psi_{B\beta}^{A\alpha}$ maps:

$$t_A^i = J_{B\beta j}^{A\alpha i} t_B^j = C_{B\beta j}^{A\alpha i} t_B^j. \tag{10}$$

(c) The Jacobian matrix $J_{B\beta j}^{A\alpha i}$ and its dual $J_{A\alpha i}^{*B\beta j}$ are inverses

$$\delta_{Aj}^{Ai} = J_{B\beta k}^{A\alpha i} J_{A\alpha j}^{*B\beta k}. \tag{11}$$

This last property ensures that tensor contractions and traces transform properly under these boundary interface mappings.

The Jacobian matrices constructed in Eqs. (6) and (7) using the identification maps $\Psi_{B\beta}^{A\alpha}$ and the reference metric g_{ij} define the transformations needed to connect arbitrary tensor fields across the interface boundaries of multi-cube manifolds. These transformations make it possible therefore to define what it means for a global tensor field to be continuous on multi-cube manifolds: A tensor field is continuous on a multi-cube manifold if its multi-cube coordinate components are continuous within each region $\mathcal{B}_A$, and if its multi-cube coordinate components at each interface boundary point are equal to the transform of its components from the neighboring region.

The reference metric can also be used to define a smooth connection

$$\Gamma_{jk}^i = \frac{1}{2} g^{i\ell} (\partial_j g_{\ell k} + \partial_k g_{\ell j} - \partial_\ell g_{jk}), \tag{12}$$

that can be used to define a covariant derivative operator ∇_i. This covariant derivative is related to the coordinate partial derivatives (within each region $\mathcal{B}_A$) by the usual expressions for the case of vectors and covectors:

$$\nabla_i v^j = \partial_i v^j + \Gamma_{ik}^j v^k, \tag{13}$$

$$\nabla_i w_j = \partial_i w_j - \Gamma_{ij}^k w_k. \tag{14}$$

The covariant gradients of tensors, e.g. $\nabla_i v^j$ and $\nabla_i w_j$, are themselves tensor fields. Therefore they are transformed at interface boundaries using the Jacobian matrices defined in Eqs. (6) and (7) as well. Thus, for example, the gradients of vectors and covectors transform as,

$$\nabla_{Ai} v_A^j = J_{A\alpha i}^{*B\beta k} J_{B\beta \ell}^{A\alpha j} \nabla_{Bk} v_B^\ell, \tag{15}$$

$$\nabla_{Ai} w_{Aj} = J_{A\alpha i}^{*B\beta k} J_{A\alpha j}^{*B\beta \ell} \nabla_{Bk} w_{B\ell}. \tag{16}$$

Using these transformation laws it is straightforward to define what it means for a global tensor field to be differentiable on a multi-cube manifold: A tensor field is differentiable if the tensor and its covariant gradient are continuous everywhere including across all multi-cube interfaces. The concept of C^k tensors can be built up in a straightforward way simply by taking kth order covariant gradients of tensors and demanding that the tensor and all gradients up through kth order be continuous global tensor fields.

The addition of a smooth (i.e. C^k differentiable) positive definite reference metric g_{ij} therefore provides all the additional information needed to define a global C^k differential structure on any multi-cube manifold.

4. Interface boundary conditions for multi-cube manifolds

The multi-cube representations of manifolds provide a practical framework in which to solve systems of partial differential equations numerically on manifolds with non-trivial spatial topologies. The idea is to solve those equations on each of the cubic regions $\mathcal{B}_A$, using boundary conditions on the faces $\partial_\alpha \mathcal{B}_A$ that ensure the combination of local solutions from each region satisfies the system of equations globally—including at the boundaries. Solving differential equations using multi-patch methods is a common practice in computational physics on manifolds that are subsets of R^3 [4–10]. Such methods are used for example in the pseudo-spectral code SpEC (developed by the Caltech/Cornell numerical relativity collaboration [15–19]) to solve Einstein's equations. The multi-cube framework developed here extends the class of problems accessible to such codes by allowing them to solve problems on computational domains that cannot be covered by a single global coordinate chart. This generalization provides a method of solving differential equations on two-dimensional and three-dimensional manifolds with arbitrary topologies, in addition to a very large class of higher dimensional manifolds. The code changes needed to implement these more general multi-cube methods require fairly minor generalizations of the way boundary conditions are imposed at the interfaces between cubic regions in standard multi-patch codes. The needed generalizations are described here in some detail for second-order quasi-linear strongly-elliptic and first-order symmetric-hyperbolic systems of equations.

4.1. Interface boundary conditions for elliptic systems

A second-order quasi-linear strongly-elliptic system of equations for a collection of tensor fields u^A can be written in the form

$$\nabla_j[M^{jkA}{}_B(\mathbf{u})\nabla_k u^B] = F^B(\mathbf{u}, \nabla\mathbf{u}), \tag{17}$$

where ∇_i is some covariant derivative operator, $M^{jkA}{}_B(\mathbf{u})$ may depend on the fields but not their derivatives, and $F^B(\mathbf{u}, \nabla\mathbf{u})$ may depend on the fields and their first derivatives. The script indexes $\mathcal{A}, \mathcal{B}, \mathcal{C}, \ldots$ in these expressions label the components of the collection of tensor fields that make up u^A. Such a system is strongly elliptic if there is a positive definite metric on the space of fields, S_{AB}, a positive definite spatial metric, g^{ij}, on the manifold (e.g. the reference metric used to define the multi-cube structure) and a positive constant, $C > 0$, such that

$$w_j w_k M^{jkC}{}_A S_{CB} v^A v^B \geqslant C g^{jk} w_j w_k S_{AB} v^A v^B, \tag{18}$$

for every v^A and every w_j [20].

All differentiable solutions to second-order elliptic systems of this type are smooth, assuming the quantities M^{jkA}_B and F^B are smooth [20]. Boundary conditions for these equations at internal inter-region boundaries are therefore quite simple: the solutions u^A and their normal derivatives $n^i \nabla_i u^A$ (where n^i is the normal to the boundary) must be continuous when transformed appropriately across inter-region boundaries.[2]

These continuity conditions can only be imposed at the interface boundaries by transforming the fields u^A computed in one region, $\mathcal{B}_B$, into the tensor basis used by its neighboring region, $\mathcal{B}_A$. The fields u^A are (by assumption) a collection of tensor fields whose components are transformed across region boundaries using the Jacobian as defined in Eqs. (3) and (4). Thus the fields u^A_B (expressed in the tensor basis associated with the coordinates x^i_B from the region $\mathcal{B}_B$) are related to the fields u^A_A (in the tensor basis associated with the coordinates x^i_A from the region $\mathcal{B}_A$) by a transformation of the form,

$$u^A_A = \mathcal{J}^A_B u^B_B, \tag{19}$$

where $\mathcal{J}^A_B$ is the multi-component Jacobian appropriate for each tensor part of u^B. For example, a system whose fields consist of a scalar, a vector, and a covector $u^B = \{\psi, v^i, w_i\}$, would transform as follows,

$$\mathcal{J}^A_B u^B = \left\{ \psi_B, J^{A\alpha j}_{B\beta i} v^i_B, J^{*B\beta i}_{A\alpha j} w_{Bi} \right\}. \tag{20}$$

---

[2] It is easy to see that the continuity of the fields u^A and their normal derivatives $n^i \nabla_i u^A$ must both be imposed as internal interface boundary conditions for second-order elliptic systems. Consider a computational domain $\mathcal{D}$ on which an elliptic system along with suitable boundary conditions is to be solved. Now consider dividing this domain into two subdomains, $\mathcal{D} = \mathcal{D}_1 \cup \mathcal{D}_2$, separated by an internal interface boundary. A solution to this elliptic system is determined within each of these subdomains by specifying (arbitrarily) the values of the fields on this interface boundary (in addition to the outer boundary conditions on the original domain $\mathcal{D}$). The normal derivatives of the fields in these solutions will not in general be continuous across the interface, however, so these solutions will not in general equal the desired global solution on $\mathcal{D}$. The correct global solution is only determined, therefore, by requiring continuity of both the fields and their normal derivatives at internal interface boundaries.

The boundary conditions for second-order elliptic systems also place conditions on the normal derivatives of the fields, $n^i \nabla_i u^A$. The covariant gradient of a tensor field is itself a tensor field, so these gradients are transformed across region boundaries by an equation analogous to Eq. (19):

$$\nabla_{Ai} u_A^A = J_{A\alpha i}^{*B\beta j} \mathcal{J}_\mathcal{B}^A \nabla_{Bj} u_B^\mathcal{B}. \tag{21}$$

It may be more convenient in some cases to impose the needed continuity conditions on the partial derivatives, $n^i \partial_i u^A$, rather than the covariant derivatives of the fields, $n^i \nabla_i u^A$. The interface boundary transformations needed in this case are easy to obtain from Eq. (21): the covariant derivatives ∇_{Ak} and ∇_{Bk} that appear in this condition are re-expressed in terms of the partial derivatives ∂_{Ai} and ∂_{Ai}, and the connection coefficients Γ_{Ajk}^i and Γ_{Bjk}^i. For the case of vector and co-vector fields, the resulting partial derivative transformation laws are given by,

$$\partial_{Ak} v_A^i = J_{A\alpha k}^{*B\beta \ell} J_{B\beta j}^{A\alpha i} \partial_{B\ell} v_B^j + \left(J_{A\alpha k}^{*B\beta \ell} J_{B\beta n}^{A\alpha i} \Gamma_{B\ell j}^n - J_{B\beta j}^{A\alpha n} \Gamma_{Akn}^i \right) v_B^j, \tag{22}$$

$$\partial_{Ak} w_{Ai} = J_{A\alpha k}^{*B\beta \ell} J_{A\alpha i}^{*B\beta j} \partial_{B\ell} v_{Bj} - \left(J_{A\alpha k}^{*B\beta \ell} J_{A\alpha i}^{*B\beta n} \Gamma_{B\ell n}^j - J_{A\alpha n}^{*B\beta j} \Gamma_{Aki}^n \right) w_{Bj}. \tag{23}$$

The needed interface boundary conditions for second-order elliptic systems can now be stated precisely: Let $\mathcal{B}_A$ and $\mathcal{B}_B$ represent cubic regions whose faces $\partial_\alpha \mathcal{B}_A$ and $\partial_\beta \mathcal{B}_B$ are identified. Let u_A^A and u_B^A denote the fields evaluated in the cubic regions $\mathcal{B}_A$ and $\mathcal{B}_B$ respectively. The required interface boundary conditions can then be written as,

$$u_B^\mathcal{B} = \mathcal{J}_A^\mathcal{B} u_A^A, \tag{24}$$

to be imposed on the boundary face $\partial_\beta \mathcal{B}_B$, and the equation,

$$n_A^i \nabla_{Ai} u_A^A = n_A^i J_{A\alpha i}^{*B\beta k} \mathcal{J}_\mathcal{B}^A \nabla_{Bk} u_B^\mathcal{B}, \tag{25}$$

to be imposed on the boundary face $\partial_\alpha \mathcal{B}_A$.

The required continuity conditions can be imposed numerically by replacing the elliptic system, Eq. (17), with the equation for the continuity of the fields on the grid points of one of the boundary faces, $\partial_\beta \mathcal{B}_B$, and the equation for the continuity of the normal derivatives on the grid points of the other face $\partial_\alpha \mathcal{B}_A$. Together these boundary conditions ensure that the global solution to Eq. (17) will have the required continuity and differentiability at interface boundaries. Second-order strongly-elliptic systems can be solved using either Dirichlet or Neumann type boundary conditions. Thus the continuity conditions imposed here are exactly those needed to ensure the well-posedness of the boundary value problem within each cubic region.

Boundary conditions of this type are already used successfully and routinely in elliptic-solver codes that implement traditional multi-patch methods (see e.g. Ref. [16]). The only difference between the boundary conditions used in those traditional multi-patch codes and the ones introduced here is the form of the Jacobian matrices used to transform the components of tensors and their derivatives at the interfaces between regions. In traditional multi-patch methods these Jacobians are just identity matrices, because in those cases there was always a smooth global coordinate basis that could be used to represent tensor fields in all computational subdomains. In the multi-cube method introduced here, these Jacobians contain critical information about the differential topology of the manifold.

4.2. Interface boundary conditions for hyperbolic systems

A first-order symmetric-hyperbolic system of equations for the dynamical fields u^A (assumed here to be a collection of tensor fields) can be written in the form

$$\partial_t u^A + A^{kA}{}_\mathcal{B}(\mathbf{u}) \nabla_k u^\mathcal{B} = F^A(\mathbf{u}), \tag{26}$$

where the characteristic matrix, $A^{kA}{}_\mathcal{B}(\mathbf{u})$, and source term, $F^A(\mathbf{u})$, may depend on the fields u^A but not their derivatives. The script indexes $\mathcal{A}, \mathcal{B}, \mathcal{C}, \ldots$ in these expressions label the components of the collection of tensor fields that make up u^A. These systems are called symmetric because, by assumption, there exists a positive definite metric on the space of fields, $S_{\mathcal{AB}}$, that can be used to transform the characteristic matrix into a symmetric form: $S_{\mathcal{AC}} A^{k\mathcal{C}}{}_\mathcal{B} \equiv A_{\mathcal{AB}}^k = A_{\mathcal{BA}}^k$.

Boundary conditions for symmetric-hyperbolic systems must be imposed on the incoming characteristic fields of the system. The characteristic fields $\hat{u}^\mathcal{K}$ (whose index $\mathcal{K}$ labels the collection of characteristic fields) are projections of the dynamical fields u^A onto the left eigenvectors of the characteristic matrix (cf. Refs. [21,22]),

$$\hat{u}^\mathcal{K} = e_\mathcal{A}^\mathcal{K}(\mathbf{n}) u^A, \tag{27}$$

defined by the equation,

$$e_\mathcal{A}^\mathcal{K}(\mathbf{n}) n_k A^{k\mathcal{A}}{}_\mathcal{B}(u) = v_{(\mathcal{K})} e_\mathcal{B}^\mathcal{K}(\mathbf{n}). \tag{28}$$

The co-vector n_k that appears in this definition is the outward pointing unit normal to the surface on which the characteristic fields are evaluated. The eigenvalues $v_{(\mathcal{K})}$ are often referred to as the characteristic speeds of the system. The characteristic fields $\hat{u}^\mathcal{K}$ represent the independent dynamical degrees of freedom at the boundaries. These characteristic fields propagate at

the speeds $v_{(\mathcal{K})}$ (in the short wavelength limit), so boundary conditions must be given for each incoming characteristic field, i.e. for each field with speed $v_{(\mathcal{K})} < 0$. No boundary condition is required (or allowed) for outgoing characteristic fields, i.e. for any field with $v_{(\mathcal{K})} \geqslant 0$.

The boundary conditions on the dynamical fields u^A that ensure the equations are satisfied across the faces of adjoining cubic regions are quite simple: data for the incoming characteristic fields at the boundary of one region are supplied by the outgoing characteristic fields from the neighboring region. The boundary conditions at an interface between cubic regions require that the dynamical fields u_A^A in region $\mathcal{B}_A$ be transformed into the tensor basis used in the neighboring region $\mathcal{B}_B$. When the dynamical fields u^A are a collection of tensor fields (as assumed here) their components are transformed from one coordinate representation to another using the Jacobian of the transformation as described in Eq. (19). In this case the needed boundary conditions can be stated precisely for hyperbolic evolution problems: Consider two cubic regions $\mathcal{B}_A$ and $\mathcal{B}_B$ whose boundaries $\partial_\alpha \mathcal{B}_A$ and $\partial_\beta \mathcal{B}_B$ are identified by the map $\Psi_{\beta B}^{\alpha A}$ as defined in Eq. (1). The required boundary conditions on the dynamical fields u_A^A consist of fixing the incoming characteristic fields $\hat{u}_A^{\mathcal{K}}$, i.e. those with speeds $v_{(\mathcal{K})} < 0$, at the boundary $\partial_\alpha \mathcal{B}_A$ with data, u_B^B, from the fields on the neighboring boundary $\partial_\beta \mathcal{B}_B$:

$$\hat{u}_A^{\mathcal{K}} = e_A^{\mathcal{K}}(\mathbf{n}) \mathcal{J}_B^A u_B^B. \tag{29}$$

The matrix of eigenvectors, $e_A^{\mathcal{K}}(\mathbf{n})$, that appears in this expression is to be evaluated using the fields from region $\mathcal{B}_B$ that have been transformed into region $\mathcal{B}_A$ where the boundary condition is to be imposed. This boundary condition must be applied to each incoming characteristic field on each internal cube face, i.e. on each face that is identified with the face of a neighboring region.

This type of boundary condition is used routinely and successfully by hyperbolic evolution codes, such as the Caltech/Cornell SpEC code, that implement traditional multi-patch methods. Those traditional applications differ from the multi-cube methods discussed here only in the fact that tensors in those traditional cases could always be expressed in terms of the global coordinate basis. The generalized Jacobians $\mathcal{J}_B^A$ needed to transform tensors across interface boundaries in those traditional applications of multi-patch methods are therefore just the identity map. In the more general multi-cube construction introduced in Sections 2 and 3 the Jacobians contain critical information about the differential topology of the manifold, so the transformations used here must be slightly more complicated than those used in the traditional multi-patch case. Other than that simple difference, however, the boundary conditions introduced here are the same as those used in the traditional multi-patch methods.

In some cases, like systems representing second-order tensor wave equations, the dynamical fields will include a collection of primary tensor fields plus a collection of secondary fields representing the first derivatives of the primary fields. In most cases the secondary fields can be defined using a covariant derivative, thus making them tensor fields as well. The Einstein equations are somewhat problematic, because the most natural covariant derivative of the metric tensor (the primary tensor field in this case) vanishes identically. Thus first-order symmetric-hyperbolic representations of the Einstein equations are not generally co-variant [22]. They can be made fully covariant however by defining the secondary dynamical fields using the covariant derivative associated with the non-dynamical reference metric that defines the differential topology of the manifold. This type of fully covariant first-order representation of the Einstein system will be discussed in detail in a future publication.

5. Numerical tests of a multi-cube elliptic equation solver

This section discusses a series of tests of the numerical solution of elliptic equations on compact three-manifolds using the multi-cube methods described in Sections 2–4. These tests find numerical solutions to the equation

$$\nabla^i \nabla_i \psi - c^2 \psi = f, \tag{30}$$

where ψ is a scalar field, ∇_i represents the covariant derivative associated with a fixed smooth positive-definite metric g_{ij} on a particular three-manifold, c is a constant, and f is a fixed source function. The constant term, with $c^2 > 0$, ensures the solution to this equation is unique on any compact three-manifold. This equation is solved here on the three-manifolds whose multi-cube representations are described in Appendix A: T^3 with a flat metric, $S^2 \times S^1$ with a round constant-curvature metric, and S^3 with the standard round constant-curvature metric. The source functions f for these tests are chosen to ensure that the solutions ψ are non-trivial functions which are known analytically.

The accuracy and effectiveness of the numerical solutions of Eq. (30) are evaluated in two ways. The first accuracy indicator used here is the residual, R, which measures how well the numerical solutions satisfy the discrete form of the differential equations. This numerical residual is defined as

$$R = \nabla^i \nabla_i \psi_N - c^2 \psi_N - f, \tag{31}$$

where ψ_N is the numerical solution of the discrete form of Eq. (30). The size of this residual is monitored for each numerical solution by evaluating its L^2 norm and computing the normalized residual error quantity, $\mathcal{E}_R$, defined as

$$\mathcal{E}_R = \sqrt{\frac{\int R^2 \sqrt{g} \, d^3 x}{\int f^2 \sqrt{g} \, d^3 x}}. \tag{32}$$

The second accuracy indicator used here measures the error in the numerical solution itself: $\Delta\psi = \psi_E - \psi_N$, where ψ_E and ψ_N represent the exact analytical solution and the discrete numerical solutions respectively. The magnitude of $\Delta\psi$ is evaluated using the scale invariant L^2 measure of the solution error:

$$\mathcal{E}_\psi = \sqrt{\frac{\int (\Delta\psi)^2 \sqrt{g}\, d^3x}{\int \psi_E^2 \sqrt{g}\, d^3x}}. \tag{33}$$

The numerical tests described here were performed using the elliptic equation solver that is part of the SpEC code [16]. This code, developed originally by the Caltech/Cornell numerical relativity collaboration, uses pseudo-spectral methods to represent functions and to evaluate their spatial derivatives. It evaluates the residual (and its linearization for non-linear problems) for the elliptic system numerically, e.g. Eq. (31) with boundary conditions replacing the elliptic system at boundary collocation points. The code solves the linearized equations and uses the linearized solution to reduce the size of the full non-linear residual via Newton–Raphson like methods. The minimization of both the linearized and non-linear residuals (including interface boundary terms) are done in parallel on all of the computational regions, so the resulting minimizing field represents an approximate global numerical solution to the original global elliptic system. The SpEC code uses the PETSc toolkit of linear and non-linear equation solvers to perform these residual minimization procedures, as described in more detail Ref. [16].

Each cubic region in the tests described here is subdivided into one or more computational subregions, on which the field components are fixed at the Gauss–Lobatto collocation points, and derivatives are computed using Chebyshev expansions. The structure of these subregions was chosen to achieve fairly uniform spatial resolution. The particular choice of subregions is described in the discussion of each test.

These numerical tests verify that several new ideas introduced in Sections 2–4 and Appendix A are correct, and that these ideas have been implemented correctly in the SpEC code. The most fundamental new ideas tested here are the inter-region boundary conditions, Eqs. (24) and (25), for elliptic equations. These internal boundary conditions depend on the Jacobians and their derivatives, which depend in turn on the inter-region boundary maps in a critical way for manifolds with non-trivial topologies. These Jacobian terms contribute to the boundary conditions in a non-trivial way even for the simple scalar elliptic Eq. (30) used in these tests. These tests also depend in a non-trivial way on the multi-cube representations of the reference metrics Eqs. (A.9) and (A.20) and their associated covariant derivatives on the manifolds $S^2 \times S^1$ and S^3. If any of these new elements of the multi-cube method were incorrect (or were implemented incorrectly in the code) the numerical tests described here would not achieve the exponential convergence in the solution error measure $\mathcal{E}_\psi$ that is seen in these tests.

5.1. Tests of a multi-cube elliptic equation solver on T^3

The numerical tests described here use the multi-cube representation of the three-manifold with topology T^3 given in Appendix A.1. The reference metric in this case is the flat Euclidean metric, Eq. (A.1), so the covariant derivatives which appear in the elliptic Eq. (30) are just the Cartesian coordinate partial derivatives. When written in terms of the multi-cube Cartesian coordinates on T^3, therefore, this equation takes the simple form,

$$\nabla^i\nabla_i\psi - c^2\psi = \partial_x^2\psi + \partial_y^2\psi + \partial_z^2\psi - c^2\psi = f. \tag{34}$$

This equation is solved numerically in these tests using the source function f given by,

$$f(x,y,z) = -(\omega^2 + c^2)\cos\left[\frac{2\pi}{L}(kx + \ell y + mz)\right], \tag{35}$$

where k, ℓ, and m are integers, c is a constant $c = 1/L$, and ω is given by

$$\omega^2 = \left(\frac{2\pi}{L}\right)^2 (k^2 + \ell^2 + m^2). \tag{36}$$

The exact analytical solution to this equation is given by

$$\psi_E(x,y,z) = \cos\left[\frac{2\pi}{L}(kx + \ell y + mz)\right]. \tag{37}$$

The numerical tests of the solutions to Eqs. (34)–(36) were performed using a source function with $k = \ell = m = 2$. These tests were performed on a set of eight computational subregions using a range of numerical resolutions having $N = 8, 10, 12, 14, 16, 18$ and 20 collocation points respectively in each spatial direction in each subregion. These subregions divide the one cubic region $\mathcal{B}_1$ needed to represent T^3 into eight cubes: each half the size of the region in each spatial direction. The internal boundary maps between these subregions are just the trivial identity maps. The graphs of the solution errors $\mathcal{E}_\psi$ and the residual errors $\mathcal{E}_\mathcal{R}$, as defined in Eqs. (32) and (33), for these tests are shown in Fig. 4. The elliptic solver for these tests were

run until the residual errors $\mathcal{E}_\mathcal{R}$ were reduced to the level of numerical roundoff. These results demonstrate that the boundary conditions introduced here on region boundaries were implemented correctly and efficiently: successfully achieving the exponential convergence expected of spectral numerical methods.

5.2. Tests of a multi-cube elliptic equation solver on $S^2 \times S^1$

The numerical tests described here use the multi-cube representation of the three-manifold with topology $S^2 \times S^1$ given in Appendix A.2. The reference metric used in this case is the constant-curvature round metric given in terms of angular coordinates $\{\chi, \theta, \varphi\}$ in Eq. (A.8), and in the multi-cube Cartesian coordinates used in these tests in Eq. (A.9). This choice of reference metric makes the elliptic Eq. (A.9) somewhat more complicated in this case. In terms of the standard angular coordinates this equation has the form

$$\nabla^i \nabla_i \psi - c^2 \psi = \frac{\partial_\chi^2 \psi}{R_1^2} + \frac{\partial_\theta[\sin\theta \partial_\theta \psi]}{R_2^2 \sin\theta} + \frac{\partial_\varphi^2 \psi}{R_2^2 \sin^2\theta} - c^2 \psi = f. \tag{38}$$

This equation is solved numerically in these tests with a source function f given by,

$$f(\chi, \theta, \varphi) = -(\omega^2 + c^2)\Re[e^{ik\chi} Y_{\ell m}(\theta, \varphi)], \tag{39}$$

where $Y_{\ell m}(\theta, \varphi)$ is the standard S^2 spherical harmonic function, k, ℓ, and m are integers, c is a constant $c = 1/R_2$, ω is given by

$$\omega^2 = \frac{\ell(\ell+1)}{R_2^2} + \frac{k^2}{R_1^2}, \tag{40}$$

and $\Re[Q]$ denotes the real part of a quantity Q. The exact analytical solution to this equation is given by

$$\psi_E(\chi, \theta, \varphi) = \Re[e^{ik\chi} Y_{\ell m}(\theta, \varphi)]. \tag{41}$$

The numerical solution to this equation is carried out using the Cartesian coordinates of the multi-cube description of $S^2 \times S^1$ described in Appendix A.2. The covariant derivatives used by the SpEC code for this test are evaluated using the Cartesian coordinate representation of the round metric given in Eq. (A.9). The source function f that appears on the right side of Eq. (38), is evaluated in the multi-cube Cartesian coordinates used for these tests with the transformations between the angular and Cartesian coordinates given in Tables A.4 and A.5.

The tests performed here used the source function given in Eqs. (39) and (40) with $k = \ell = m = 2$. These tests used a set of twelve computational subregions to represent the six cubic regions of $S^2 \times S^1$, cf. Fig. A.10. These subregions divide each region in the periodically identified z direction into two subregions. These tests were performed using $N = 8, 10, 12, 14, 16, 18, 20$ and 22 collocation points respectively in each spatial direction in each of the computational subregions. The boundary conditions at the inter-region boundaries are based on the maps specified in Table A.3. The graphs of the solution errors $\mathcal{E}_\psi$ and the residual errors $\mathcal{E}_\mathcal{R}$, as defined in Eqs. (32) and (33), for these tests are shown in Fig. 5. The elliptic solver for these tests were run until the residual errors $\mathcal{E}_\mathcal{R}$ were reduced to the level of numerical roundoff. This graph demonstrates, for the non-trivial $S^2 \times S^1$ case, that the computational region boundary conditions developed here have been implemented correctly and efficiently, achieving the exponential convergence expected of spectral numerical methods.

5.3. Tests of a multi-cube elliptic equation solver on S^3

The numerical tests described here use the multi-cube representation of the three-manifold with topology S^3 given in Appendix A.3. The reference metric used in this case is the standard constant-curvature round metric for S^3 given in terms
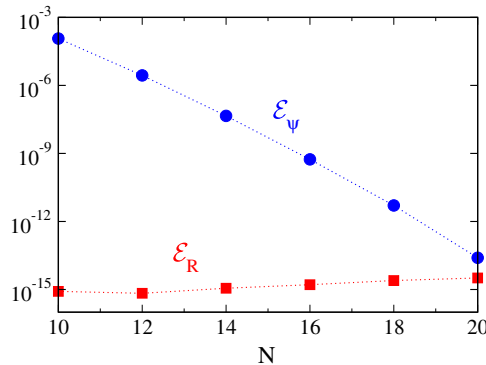
Fig. 4. Errors in the numerical solutions $\Delta\psi$ of the elliptic Eq. (34) on T^3 with $k = \ell = m = 2$, as quantified by the error measures $\mathcal{E}_\psi$ and $\mathcal{E}_\mathcal{R}$. The parameter N is the number of collocation points used for these tests in each spatial direction in each computational subregion.
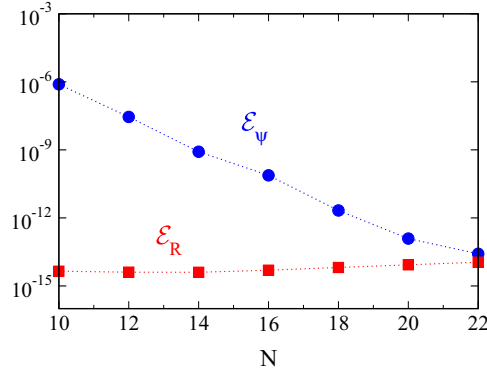
Fig. 5. Errors in the numerical solutions $\Delta\psi$ of the elliptic Eq. (38) on $S^2 \times S^1$ with $k = \ell = m = 2$, as quantified by the error measures $\mathcal{E}_\psi$ and $\mathcal{E}_\mathcal{R}$. The parameter N is the number of collocation points used for these tests in each spatial direction in each computational subregion.

of angular coordinates $\{\chi, \theta, \varphi\}$ in Eq. (A.19), in the multi-cube Cartesian coordinates used in these tests in Eq. (A.20). This choice of reference metric fixes the elliptic Eq. (30) to have the form,

$$\nabla^i \nabla_i \psi - c^2 \psi = \frac{\partial_\chi [\sin^2 \chi \partial_\chi \psi]}{R_3^2 \sin^2 \chi} + \frac{\partial_\theta [\sin \theta \partial_\theta \psi]}{R_3^2 \sin \theta \sin^2 \chi} + \frac{\partial_\varphi^2 \psi}{R_3^2 \sin^2 \theta \sin^2 \chi} - c^2 \psi = f, \tag{42}$$

when expressed in terms of the standard angular coordinates $\{\chi, \theta, \varphi\}$ used on S^3. The source function f used in these numerical tests is given by,

$$f(\chi, \theta, \varphi) = -(\omega^2 + c^2) \Re[Y_{k\ell m}(\chi, \theta, \varphi)], \tag{43}$$

where the $Y_{k\ell m}(\chi, \theta, \varphi)$ are the S^3 spherical harmonics described in Appendix B, k, ℓ, and m are integers, c is a constant $c = 1/R_3$, and ω is given by

$$\omega^2 = \frac{k(k+2)}{R_3^2}. \tag{44}$$

The exact analytical solution to this equation is given by

$$\psi_E(\chi, \theta, \varphi) = \Re[Y_{k\ell m}(\chi, \theta, \varphi)]. \tag{45}$$

The numerical solutions of Eq. (42) are carried out for these tests using the multi-cube representation of S^3 described in Appendix A.3. The covariant derivatives used by the SpEC code for this test are evaluated using the multi-cube Cartesian coordinate representation of the round metric on S^3 given in Eq. (A.20). The source function f, defined in Eq. (43), is evaluated in terms of the multi-cube Cartesian coordinates for these tests using the transformations between the angular and the Cartesian coordinates given in Tables A.8 and A.9.

The numerical tests described here solved the elliptic Eqs. (42)–(44) with the parameter values $k = \ell = m = 2$ in the source function f. These tests were done using a set of eight computational subregions, corresponding to the eight cubic regions needed to represent S^3, cf. Fig. A.11. These tests used $N = 8$, 10, 12, 14, 16, 18, 20 and 22 collocation points respectively in each spatial direction in each of the computational subregions. The boundary conditions at the region boundaries for these tests are based on the interface identification maps specified in Table A.8. The graphs of the solution errors $\mathcal{E}_\psi$ and the residual errors $\mathcal{E}_\mathcal{R}$, defined in Eqs. (32) and (33), for these tests are shown in Fig. 6. The elliptic solver for these tests were run until the residual errors $\mathcal{E}_\mathcal{R}$ were reduced to the level of numerical roundoff. This graph demonstrates for another non-trivial example that the inter-region boundary conditions developed here have been implemented correctly and efficiently. Fig. 6 also demonstrates that these numerical tests have achieved the exponential convergence expected of spectral numerical methods.

6. Numerical tests of a multi-cube hyperbolic equation solver

This section discusses numerical tests of the multi-cube methods for solving hyperbolic evolution equations on compact three-manifolds as described in Sections 2–4. These tests find numerical solutions to the scalar wave equation

$$-\partial_t^2 \psi + \nabla^i \nabla_i \psi = 0, \tag{46}$$

where ∇_i represents the spatial covariant derivative on the fixed geometry of the spatial three-manifold. This equation is solved here on the three-manifolds described in Appendix A: T^3 with a flat metric, $S^2 \times S^1$ with the constant curvature round metric, and S^3 with the standard constant-curvature round metric.
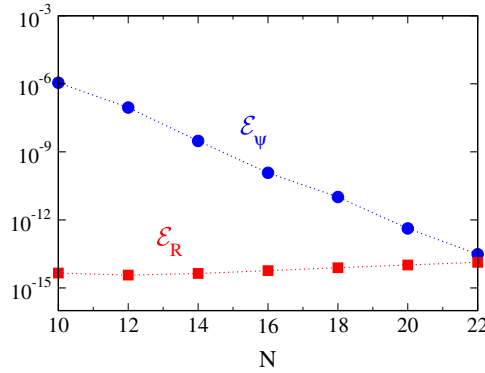
Fig. 6. Errors in the numerical solutions $\Delta\psi$ of the elliptic Eq. (42) on S^3 with $k = \ell = m = 2$ as quantified by the error measures $\mathcal{E}_\psi$ and $\mathcal{E}_R$. The parameter N is the number of collocation points used for these tests in each spatial direction in each computational subregion.

These wave equations are converted to first-order symmetric-hyperbolic form before solving them numerically. The list of dynamical fields $u^\alpha = \{\psi, \Pi, \Phi_i\}$ is therefore expanded to include the first derivatives of ψ: $\Pi = -\partial_t\psi$, and $\Phi_i = \partial_i\psi$. Constraint damping is used to enforce the constraint,

$$\mathcal{C}_i \equiv \partial_i\psi - \Phi_i = 0, \tag{47}$$

using the methods developed in Ref. [23] with constraint damping parameter $\gamma_2 = 1$.

Exact analytical solutions exist to these wave equations on the three-manifolds used in these tests. Therefore the effectiveness and efficiency of the evolution code can be tested in these cases by comparing numerical solutions ψ_N to this equation with the known analytical solutions ψ_E. The accuracy, and convergence properties, of the code can be measured therefore by monitoring the L^2 norms of $\Delta\psi = \psi_E - \psi_N$ using the solution error measure defined in Eq. (33). It is also useful to monitor the constraint violation errors $\mathcal{C}_i$. This is done by constructing the constraint error measure:

$$\mathcal{E}_\mathcal{C} \equiv \sqrt{\frac{\int g^{ij}\mathcal{C}_i\mathcal{C}_j\sqrt{g}\,d^3x}{\int g^{ij}(\Phi_i\Phi_j + \partial_i\psi\partial_j\psi)\sqrt{g}\,d^3x}}. \tag{48}$$

This constraint error measure is invariant under changes in the overall scale of the solution, and to changes in the coordinates used to represent the solution.

The tests performed here use the scalar wave evolution system that is implemented as part of the SpEC code [23,24]. This code, developed originally by the Caltech/Cornell numerical relativity collaboration, uses pseudo-spectral methods to evaluate spatial derivatives, and the method of lines to approximate the hyperbolic system of partial differential equations as sets of coupled ordinary differential equations on each collocation point. These tests use an eighth order Dormand-Prince [25] algorithm to integrate the method of lines ordinary differential equations in time. Each cubic region in these tests is subdivided into one or more computational subregions, on which field components are represented using Chebyshev basis functions at the Gauss–Labatto collocation points. The structure of these subregions was chosen to achieve fairly uniform spatial resolution. The particular choice of subregions is described in the discussion of each particular test.

6.1. Tests of a multi-cube hyperbolic equation solver on T^3

The numerical tests described here use the multi-cube representation of the three-manifold with topology T^3 given in Appendix A.1. The reference metric in this case is the flat Euclidean metric, Eq. (A.1), so the spatial covariant derivatives which appear in the wave Eq. (46) are just the Cartesian coordinate partial derivatives. When written in terms of the multi-cube Cartesian coordinates on T^3, therefore, the wave equation takes the simple form,

$$-\partial_t^2\psi + \nabla^i\nabla_i\psi = -\partial_t^2\psi + \partial_x^2\psi + \partial_y^2\psi + \partial_z^2\psi = 0. \tag{49}$$

The idea is to solve this equation numerically with initial data:

$$\psi(t, x, y, z)|_{t=0} = \cos\left[\frac{2\pi}{L}(kx + \ell y + mz)\right], \tag{50}$$

$$\partial_t\psi(t, x, y, z)|_{t=0} = -\omega\sin\left[\frac{2\pi}{L}(kx + \ell y + mz)\right], \tag{51}$$

where k, ℓ, and m are integers, and ω is given by
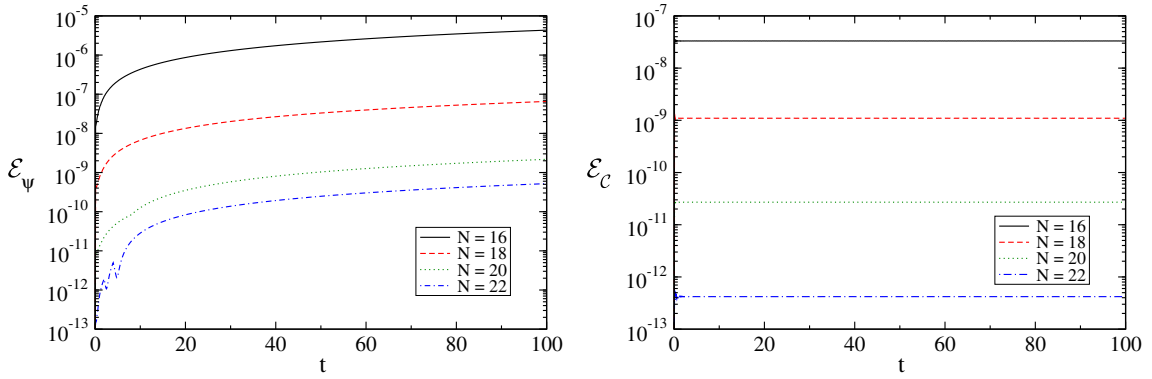
Fig. 7. Left: Errors in the numerical solutions $\Delta\psi$ for the T^3 evolutions with $k = \ell = m = 2$ as measured by the quantity $\mathcal{E}_\psi$. Right: Constraint errors $\mathcal{C}_i$ for the T^3 evolutions with $k = \ell = m = 2$ as measured by the quantity $\mathcal{E}_\mathcal{C}$.

$$\omega^2 = \left(\frac{2\pi}{L}\right)^2 (k^2 + \ell^2 + m^2). \tag{52}$$

The exact solution to this initial value problem is given analytically by

$$\psi_E(t, x, y, z) = \cos\left[\omega t + \frac{2\pi}{L}(kx + \ell y + mz)\right]. \tag{53}$$

The numerical solution of the wave Eq. (49) for these tests was performed on a set of eight computational subregions. These subregions divide the one cubic region needed to represent T^3 into eight cubes, each half the size of the region in each spatial direction. The internal boundary maps between these subregions are just the trivial identity maps. These hyperbolic evolution tests were performed using the initial data given in Eqs. (50) and (51) with $k = \ell = m = 2$. These tests used computational subregions having $N = 16$, 18, 20 and 22 collocation points respectively in each spatial direction. The graphs of the solution errors $\mathcal{E}_\psi$ and the constraint violation errors $\mathcal{E}_\mathcal{C}$ for these tests are shown in Fig. 7. These graphs demonstrate that the numerical methods described here successfully achieve the exponential convergence expected of spectral numerical methods. The slow growth in time of the solution error $\mathcal{E}_\psi$, seen in the left side of Fig. 7 is linear in time. This type of error is a common feature of the ordinary differential equation integrator used for these tests.

6.2. Tests of a multi-cube hyperbolic equation solver on $S^2 \times S^1$

The numerical tests described here use the multi-cube representation of the three-manifold with topology $S^2 \times S^1$ given in Appendix A.2. The reference metric used in this case is the constant-curvature round metric given in terms of angular coordinates $\{\chi, \theta, \varphi\}$ in Eq. (A.8), and in the multi-cube Cartesian coordinates used in these tests in Eq. (A.9). This choice of reference metric fixes the wave Eq. (30) to have the form

$$-\partial_t^2\psi + \nabla^i\nabla_i\psi = -\partial_t^2\psi + \frac{\partial_\chi^2\psi}{R_1^2} + \frac{\partial_\theta[\sin\theta\partial_\theta\psi]}{R_2^2\sin\theta} + \frac{\partial_\varphi^2\psi}{R_2^2\sin^2\theta} = 0, \tag{54}$$

when expressed in terms of the angular coordinates $\{\chi, \theta, \varphi\}$ used on $S^2 \times S^1$. The idea is to solve this equation numerically with initial data:

$$\psi(t, \theta, \varphi, \chi)_{t=0} = \Re[e^{ik\chi}Y_{\ell m}(\theta, \varphi)], \tag{55}$$

$$\partial_t\psi(t, \theta, \varphi, \chi)_{t=0} = \Re[i\omega e^{ik\chi}Y_{\ell m}(\theta, \varphi)], \tag{56}$$

where $Y_{\ell m}(\theta, \varphi)$ are the standard S^2 spherical harmonics, k, ℓ, and m are integers, ω is given by

$$\omega^2 = \frac{\ell(\ell+1)}{R_2^2} + \frac{k^2}{R_1^2}, \tag{57}$$

and $\Re[Q]$ denotes the real part of the quantity Q. The exact solution to this initial value problem is given analytically by

$$\psi_E(t, \theta, \varphi, \chi) = \Re[e^{i\omega t + ik\chi}Y_{\ell m}(\theta, \varphi)]. \tag{58}$$
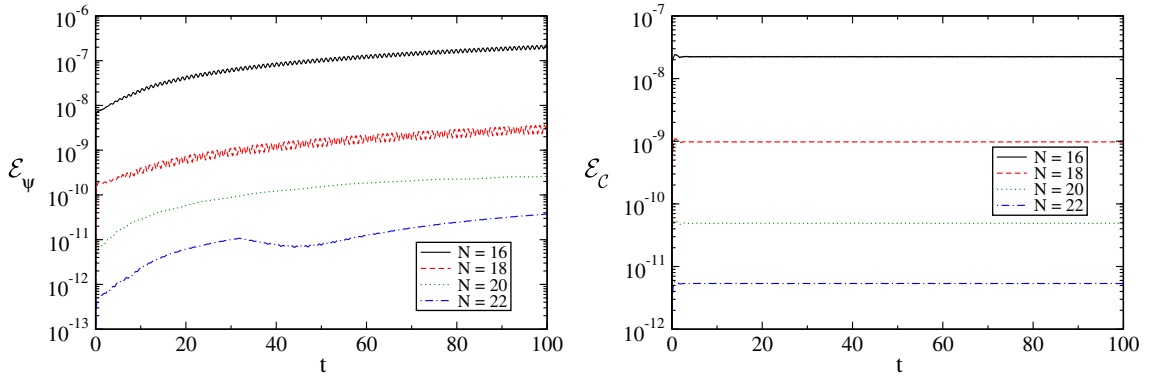
Fig. 8. Left: Errors in the numerical solutions $\Delta\psi$ for the $S^2 \times S^1$ evolutions with $k = \ell = m = 2$ as measured by the quantity $\mathcal{E}_\psi$. Right: Constraint errors $\mathcal{C}_i$ for the $S^2 \times S^1$ evolutions with $k = \ell = m = 2$ as measured by the quantity $\mathcal{E}_\mathcal{C}$.

The numerical solution of Eq. (54) is carried out using the Cartesian coordinates of the multi-cube description of $S^2 \times S^1$ described in Appendix A.2. The spatial covariant derivatives used by the SpEC code for this test are evaluated using the Cartesian coordinate representation of the round metric given in Eq. (A.9). The initial data, Eqs. (55) and (56), used for these tests are evaluated in the multi-cube Cartesian coordinates with the transformations between the angular and Cartesian coordinates given in Tables A.4 and A.5.

The numerical solution of the scalar wave Eq. (54) for these tests was performed on a set of twelve computational subregions. These subregions divide the six cubic regions needed to represent $S^2 \times S^1$, cf. Fig. A.10, into cubes that are half the size of the region in the z direction. The internal boundary maps between these subregions are just the trivial identity maps, while the maps between regions are those given in Table A.3. These hyperbolic evolution tests were performed using the initial data given in Eqs. (55) and (56) with $k = \ell = m = 2$. These tests were performed on computational subregions having $N = 16$, 18, 20 and 22 collocation points respectively in each spatial direction. The graphs of the solution errors $\mathcal{E}_\psi$ and the constraint violation errors $\mathcal{E}_\mathcal{C}$ for these tests are shown in Fig. 8. These graphs demonstrate that the numerical methods described here successfully achieve the exponential convergence expected of spectral numerical methods. The slow growth in time of the solution error $\mathcal{E}_\psi$, seen in left side of Fig. 8 is (mostly) linear in time. This growth in the error is a common feature of the ordinary differential equation integrator used for these tests.

6.3. Tests of a multi-cube hyperbolic equation solver on S^3

The numerical tests described here use the multi-cube representation of the three-manifold with topology S^3 given in Appendix A.3. The reference metric used in this case is the standard constant-curvature round metric for S^3 given in terms of angular coordinates $\{\chi, \theta, \varphi\}$ in Eqs. (55) and (56) in the multi-cube Cartesian coordinates used in these tests in Eq. (A.20). This choice of reference metric fixes the wave Eq. (46) to have the form,

$$-\partial_t^2\psi + \nabla^i\nabla_i\psi = -\partial_t^2\psi + \frac{\partial_\chi[\sin^2\chi\,\partial_\chi\psi]}{R_3^2\sin^2\chi} + \frac{\partial_\theta[\sin\theta\,\partial_\theta\psi]}{R_3^2\sin\theta\sin^2\chi} + \frac{\partial_\varphi^2\psi}{R_3^2\sin^2\theta\sin^2\chi} = 0, \tag{59}$$

when expressed in terms of the standard angular coordinates $\{\chi, \theta, \varphi\}$ used on S^3. This equation is solved numerically with initial data:

$$\psi(t, \theta, \varphi, \chi)_{t=0} = \Re[Y_{k\ell m}(\chi, \theta, \varphi)], \tag{60}$$

$$\partial_t\psi(t, \theta, \varphi, \chi)_{t=0} = \Re[i\omega Y_{k\ell m}(\chi, \theta, \varphi)], \tag{61}$$

where $Y_{k\ell m}$ is the S^3 spherical harmonic function defined in Appendix B, k, ℓ, and m are integers, and ω is given by

$$\omega^2 = \frac{k(k+2)}{R_3^2}. \tag{62}$$

The solution to this initial value problem is given analytically by

$$\psi_E(t, \theta, \varphi, \chi) = \Re[e^{i\omega t}Y_{k\ell m}(\chi, \theta, \varphi)]. \tag{63}$$

The numerical solution of Eq. (59) is carried out using the Cartesian coordinates of the multi-cube description of S^3 described in Appendix A.3. The spatial covariant derivatives used by the SpEC code for this test are evaluated using the Cartesian coordinate representation of the round metric given in Eq. (A.20). The initial data, Eqs. (60) and (61), used for these tests are evaluated in the multi-cube Cartesian coordinates with the transformations between the angular and Cartesian coordinates given in Tables A.8 and A.9.
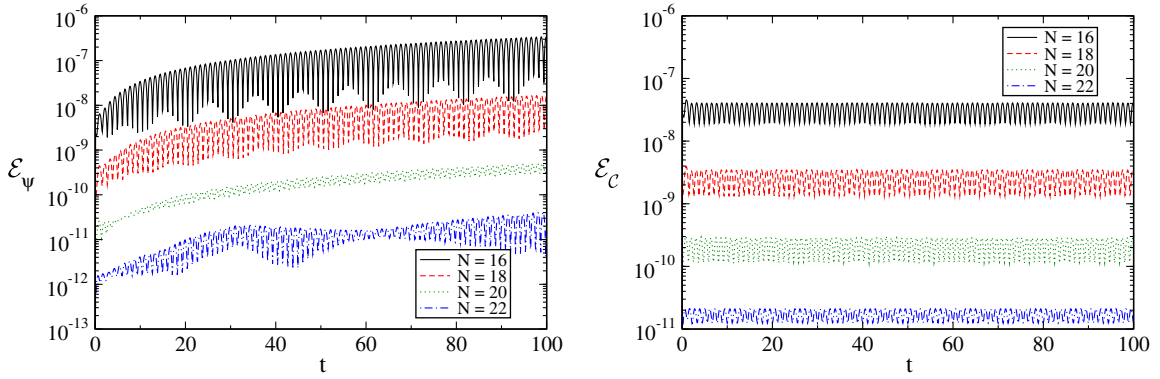
Fig. 9. Left: Errors in the numerical solutions $\Delta\psi$ for the S^3 evolutions with $k = \ell = m = 2$ as measured by the quantity $\mathcal{E}_\psi$. Right: Constraint errors $\mathcal{C}_i$ for the S^3 evolutions with $k = \ell = m = 2$ as measured by the quantity $\mathcal{E}_\mathcal{C}$.

The numerical solution of the scalar wave Eq. (59) for these tests was performed on a set of eight computational subregions. These subregions are identical to the eight cubic regions needed to represent S^3, cf. Fig. A.11. The maps between regions are those given in Table A.7. The hyperbolic evolution test was performed using the initial data given in Eqs. (60) and (61) with $k = \ell = m = 2$. These tests were performed on computational subregions having $N = 16, 18, 20$ and 22 collocation points respectively in each spatial direction. The graphs of the solution errors $\mathcal{E}_\psi$ and the constraint violation errors $\mathcal{E}_\mathcal{C}$ for these tests are shown in Fig. 9. These graphs demonstrate that the numerical methods described here successfully achieve the exponential convergence expected of spectral numerical methods. The slow growth in time of the solution error $\mathcal{E}_\psi$, seen in the left side of Fig. 9 is (mostly) linear in time. This growth in the error is a common feature of the ordinary differential equation integrator used for these tests.

Acknowledgment

Appendix A. Examples of multi-cube representations of three-manifolds

This appendix describes the construction of multi-cube representations of manifolds using the methods developed in Sections 2 and 3. Each multi-cube representation consists of a set of non-overlapping cubes $\mathcal{B}_A$ that cover the manifold, a set of maps $\Psi^{A\alpha}_{B\beta}$ that identify the faces of neighboring cubes, and finally a smooth positive definite reference metric g_{ij} used to define the differential structure on the manifold. The construction of these multi-cube structures is described here for three common three-manifolds: the three-torus T^3 with a flat reference metric, the spherical-torus $S^2 \times S^1$ with a constant-curvature round-sphere metric, and the three-sphere S^3 with the standard constant-curvature round-sphere metric. These examples are used in Sections 5 and 6 to illustrate the solution of partial differential equations on multi-cube manifolds using the methods developed in Section 4.

A.1. Multi-cube representation of T^3

The simplest example of a multi-cube manifold is the three-torus, T^3. Only a single cube $\mathcal{B}_1$ is needed to cover this manifold, and it is most convenient to locate this cube at the origin in R^3 so $\vec{c}_1 = (0, 0, 0)$. Opposite faces of this cube are identified without rotation or reflection to obtain the T^3 topology: $\partial_{+x}\mathcal{B}_1 \leftrightarrow \partial_{-x}\mathcal{B}_1$, $\partial_{+y}\mathcal{B}_1 \leftrightarrow \partial_{-y}\mathcal{B}_1$, and $\partial_{+z}\mathcal{B}_1 \leftrightarrow \partial_{-z}\mathcal{B}_1$. The maps, $\Psi^{1\pm x}_{1\mp x}$, $\Psi^{1\pm y}_{1\mp y}$, and $\Psi^{1\pm z}_{1\mp z}$, needed to effect these identifications are defined by Eq. (1) with the rotation matrices, $C^{A\alpha}_{B\beta}$, being just the identity matrices: $\mathbf{C}^{1+x}_{1-x} = \mathbf{C}^{1+y}_{1-y} = \mathbf{C}^{1+z}_{1-z} = \mathbf{I}$. The three-torus T^3 admits a smooth flat metric, so a convenient choice of reference metric for this manifold is:

$$ds^2 = g_{ij}dx^i dx^j = dx^2 + dy^2 + dz^2, \tag{A.1}$$

where x, y and z are the multi-cube Cartesian coordinates that label points in $\mathcal{B}_1$.
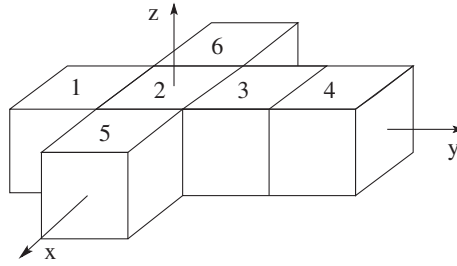
Fig. A.10. The three-manifold $S^2 \times S^1$ is represented using the six cubic regions illustrated here. The faces of these cubes are identified using the maps described in Table A.3. This representation of $S^2 \times S^1$ is based on the commonly used "cubed-sphere" representation of S^2.

Table A.2
Cube-center locations for $S^2 \times S^1$.

$\vec{c}_1 = (0, -L, 0)$	$\vec{c}_3 = (0, L, 0)$	$\vec{c}_5 = (L, 0, 0)$
$\vec{c}_2 = (0, 0, 0)$	$\vec{c}_4 = (0, 2L, 0)$	$\vec{c}_6 = (-L, 0, 0)$

Table A.3
Cube face identifications, $\partial_\alpha \mathcal{B}_A \leftrightarrow \partial_\beta \mathcal{B}_B$, and rotation matrices, $\mathbf{C}^{A\alpha}_{B\beta}$, for the interface maps in $S^2 \times S^1$. Bold face indicates the object is a matrix.

$\partial_\alpha \mathcal{B}_A \leftrightarrow \partial_\beta \mathcal{B}_B$	$\mathbf{C}^{A\alpha}_{B\beta}$	$\mathbf{C}^{B\beta}_{A\alpha}$	$\partial_\alpha \mathcal{B}_A \leftrightarrow \partial_\beta \mathcal{B}_B$	$\mathbf{C}^{A\alpha}_{B\beta}$	$\mathbf{C}^{B\beta}_{A\alpha}$
$\partial_{+z} \mathcal{B}_1 \leftrightarrow \partial_{-z} \mathcal{B}_1$	$\mathbf{I}$	$\mathbf{I}$	$\partial_{+y} \mathcal{B}_1 \leftrightarrow \partial_{-y} \mathcal{B}_2$	$\mathbf{I}$	$\mathbf{I}$
$\partial_{-y} \mathcal{B}_1 \leftrightarrow \partial_{+y} \mathcal{B}_4$	$\mathbf{I}$	$\mathbf{I}$	$\partial_{+x} \mathcal{B}_1 \leftrightarrow \partial_{-y} \mathcal{B}_5$	$\mathbf{R}_{+z}$	$\mathbf{R}_{-z}$
$\partial_{-x} \mathcal{B}_1 \leftrightarrow \partial_{-y} \mathcal{B}_6$	$\mathbf{R}_{-z}$	$\mathbf{R}_{+z}$	$\partial_{+z} \mathcal{B}_2 \leftrightarrow \partial_{-z} \mathcal{B}_2$	$\mathbf{I}$	$\mathbf{I}$
$\partial_{+y} \mathcal{B}_2 \leftrightarrow \partial_{-y} \mathcal{B}_3$	$\mathbf{I}$	$\mathbf{I}$	$\partial_{+x} \mathcal{B}_2 \leftrightarrow \partial_{-x} \mathcal{B}_5$	$\mathbf{I}$	$\mathbf{I}$
$\partial_{-x} \mathcal{B}_2 \leftrightarrow \partial_{+x} \mathcal{B}_6$	$\mathbf{I}$	$\mathbf{I}$	$\partial_{+z} \mathcal{B}_3 \leftrightarrow \partial_{-z} \mathcal{B}_3$	$\mathbf{I}$	$\mathbf{I}$
$\partial_{+y} \mathcal{B}_3 \leftrightarrow \partial_{-y} \mathcal{B}_4$	$\mathbf{I}$	$\mathbf{I}$	$\partial_{+x} \mathcal{B}_3 \leftrightarrow \partial_{+y} \mathcal{B}_5$	$\mathbf{R}_{-z}$	$\mathbf{R}_{+z}$
$\partial_{-x} \mathcal{B}_3 \leftrightarrow \partial_{+y} \mathcal{B}_6$	$\mathbf{R}_{+z}$	$\mathbf{R}_{-z}$	$\partial_{+z} \mathcal{B}_4 \leftrightarrow \partial_{-z} \mathcal{B}_4$	$\mathbf{I}$	$\mathbf{I}$
$\partial_{+x} \mathcal{B}_4 \leftrightarrow \partial_{+x} \mathcal{B}_5$	$\mathbf{R}^2_{+z}$	$\mathbf{R}^2_{+z}$	$\partial_{-x} \mathcal{B}_4 \leftrightarrow \partial_{-x} \mathcal{B}_6$	$\mathbf{R}^2_{+z}$	$\mathbf{R}^2_{+z}$
$\partial_{+z} \mathcal{B}_5 \leftrightarrow \partial_{-z} \mathcal{B}_5$	$\mathbf{I}$	$\mathbf{I}$	$\partial_{+z} \mathcal{B}_6 \leftrightarrow \partial_{-z} \mathcal{B}_6$	$\mathbf{I}$	$\mathbf{I}$

A.2. Multi-cube representation of $S^2 \times S^1$

The manifold $S^2 \times S^1$ can be covered by a set of six cubic regions $\mathcal{B}_A$ with $A = \{1, \ldots, 6\}$. A convenient way to arrange these cubes in R^3 is illustrated in Fig. A.10. The values of the cube-center location vectors $\vec{c}_A$ for this configuration is summarized in Table A.2. The inner faces of the touching cubes in Fig. A.10 are connected by identity maps, while the outer faces are identified using the maps described by Eq. (1) with the rotation matrices $\mathbf{C}^{A\alpha}_{B\beta}$ given in Table A.3. This representation of $S^2 \times S^1$ is constructed by taking the Cartesian product of S^1 (the periodically identified z-axis in this representation) with the commonly used "cubed-sphere" representation of S^2 [1–3].

It is useful to discuss the method used to construct the "cubed-sphere" representation of S^2 in some detail here, since this method is used in Appendix A.3 as the model for constructing a new representation of S^3. Let $\{\bar{x}, \bar{y}, \bar{z}\}$ denote Cartesian coordinates in an R^3, and let $\bar{x}^2 + \bar{y}^2 + \bar{z}^2 = r^2$ denote a two-sphere S^2 of radius r. It is useful for some purposes to identify points on this S^2 using standard angular coordinates θ and φ:

$$\bar{x} = r \sin\theta \cos\varphi, \tag{A.2}$$
$$\bar{y} = r \sin\theta \sin\varphi, \tag{A.3}$$
$$\bar{z} = r \cos\theta. \tag{A.4}$$

Now consider a cube $\bar{\mathcal{B}}$ centered at the origin, of size $L = 2r/\sqrt{3}$ (which just fits inside the sphere), whose orientation is aligned with the $\{\bar{x}, \bar{y}, \bar{z}\}$ axes. Let $\partial_{\bar{\alpha}} \bar{\mathcal{B}}$ represent the six faces of this cube, with $\bar{\alpha} = \pm \bar{x}$, etc., labeling the various faces. The images of these six faces can be arranged in a plane, like the $\alpha = +z$ faces of the cubes shown in Fig. A.10. The goal here is to construct a representation of $S^2 \times S^1$, so it will also be useful to make a correspondence between these cube faces $\partial_{\bar{\alpha}} \bar{\mathcal{B}}$ with the cubes shown in Fig. A.10. Table A.4 gives the relationship between the cube-face identifiers $\bar{\alpha} = \pm \bar{x}$, etc. and the cubic region labels $A = 1, 2, \ldots, 6$ shown in Fig. A.10.

Points on each of the cube-faces, $\partial_{\bar{\alpha}} \bar{\mathcal{B}}$, can be identified by their local Cartesian coordinates. For example, points on the $\bar{\alpha} = +\bar{z}$ face, i.e. the $A = 2$ face in Fig. A.10, can be identified by the coordinates $\{\bar{x}, \bar{y}\}$. It is also useful to introduce scaled local Cartesian coordinates, $\{X_A, Y_A\}$ to represent the points on these faces. For the $\bar{\alpha} = +\bar{z}$ face for example, it is useful to set

Table A.4
Cubed-Sphere Representation of S^2: Angular to Cartesian Coordinate Map.

A	$\bar{\alpha}$	X_A	Y_A
1	$-\bar{y}$	$-\frac{\bar{x}}{\bar{y}} = -\cot\varphi$	$-\frac{\bar{z}}{\bar{y}} = -\cot\theta\csc\varphi$
2	$+\bar{z}$	$\frac{\bar{x}}{\bar{z}} = \tan\theta\cos\varphi$	$\frac{\bar{y}}{\bar{z}} = \tan\theta\sin\varphi$
3	$+\bar{y}$	$\frac{\bar{x}}{\bar{y}} = \cot\varphi$	$-\frac{\bar{z}}{\bar{y}} = -\cot\theta\csc\varphi$
4	$-\bar{z}$	$-\frac{\bar{x}}{\bar{z}} = -\tan\theta\cos\varphi$	$\frac{\bar{y}}{\bar{z}} = \tan\theta\sin\varphi$
5	$+\bar{x}$	$-\frac{\bar{z}}{\bar{x}} = -\cot\theta\sec\varphi$	$\frac{\bar{y}}{\bar{x}} = \tan\varphi$
6	$-\bar{x}$	$-\frac{\bar{z}}{\bar{x}} = -\cot\theta\sec\varphi$	$-\frac{\bar{y}}{\bar{x}} = -\tan\varphi$

Table A.5
Cartesian to Angular Coordinate Map for the Cubed-Sphere Representation of S^2. The range of the local Cartesian coordinate X_A is $-1 \leqslant X_A \leqslant 1$, and the range of θ is $0 \leqslant \theta \leqslant \pi$ in these expressions. The ranges of φ for different values of Y_A are specified in the table.

A	Y_A-range	$\cos\varphi$	φ-range	$\cos\theta$
1	$-1 \leqslant Y_1 \leqslant 1$	$X_1/\sqrt{1+X_1^2}$	$\frac{7\pi}{4} \geqslant \varphi \geqslant \frac{5\pi}{4}$	$Y_1/\sqrt{1+X_1^2+Y_1^2}$
2	$1 \geqslant Y_2 \geqslant 0$	$X_2/\sqrt{X_2^2+Y_2^2}$	$\pi \geqslant \varphi \geqslant 0$	$1/\sqrt{1+X_2^2+Y_2^2}$
2	$-1 \leqslant Y_2 < 0$	$X_2/\sqrt{X_2^2+Y_2^2}$	$2\pi > \varphi \geqslant \pi$	$1/\sqrt{1+X_2^2+Y_2^2}$
3	$-1 \leqslant Y_3 \leqslant 1$	$X_3/\sqrt{1+X_3^2}$	$\frac{3\pi}{4} \geqslant \varphi \geqslant \frac{\pi}{4}$	$-Y_3/\sqrt{1+X_3^2+Y_3^2}$
4	$1 \geqslant Y_4 > 0$	$X_4/\sqrt{X_4^2+Y_4^2}$	$2\pi > \varphi \geqslant \pi$	$-1/\sqrt{1+X_4^2+Y_4^2}$
4	$-1 \leqslant Y_4 \leqslant 0$	$X_4/\sqrt{X_4^2+Y_4^2}$	$\pi \geqslant \varphi \geqslant 0$	$-1/\sqrt{1+X_4^2+Y_4^2}$
5	$-1 \leqslant Y_5 < 0$	$1/\sqrt{1+Y_5^2}$	$2\pi > \varphi \geqslant \frac{7\pi}{4}$	$-X_5/\sqrt{1+X_5^2+Y_5^2}$
5	$1 \geqslant Y_5 \geqslant 0$	$1/\sqrt{1+Y_5^2}$	$\frac{\pi}{4} \geqslant \varphi \geqslant 0$	$-X_5/\sqrt{1+X_5^2+Y_5^2}$
6	$-1 \leqslant Y_6 < 0$	$-1/\sqrt{1+Y_6^2}$	$\frac{5\pi}{4} \geqslant \varphi > \pi$	$X_6/\sqrt{1+X_6^2+Y_6^2}$
6	$1 \geqslant Y_6 \geqslant 0$	$-1/\sqrt{1+Y_6^2}$	$\pi \geqslant \varphi \geqslant \frac{3\pi}{4}$	$X_6/\sqrt{1+X_6^2+Y_6^2}$

$\{X_2, Y_2\} = \{\bar{x}/\bar{z}, \bar{y}/\bar{z}\}$. Each coordinate has been divided by $\bar{z}$, which is constant on this face, to ensure that the scaled coordinates $\{X_2, Y_2\}$ are confined to the ranges, $-1 \leqslant X_2 \leqslant 1$ and $-1 \leqslant Y_2 \leqslant 1$. Similar definitions are made on the other faces, cf. Table A.4, that ensure the X_A and Y_A are all oriented the same way as in Fig. A.10, and all satisfy $-1 \leqslant X_A \leqslant 1$ and $-1 \leqslant Y_A \leqslant 1$. Using Eqs. (A.2)–(A.4), this construction provides a natural identification between points on the original sphere, labeled by their angular coordinates $\{\theta, \varphi\}$, and the Cartesian cube-face coordinates $\{X_A, Y_A\}$ via the equations summarized in Tables A.4 and A.5.

The $\{X_A, Y_A\}$ defined in this way are local Cartesian coordinates. These could be converted to global coordinates by adding in the appropriate offset for each face: $x_A^x = c_A^x + \frac{1}{2}LX_A$ and $x_A^y = c_A^y + \frac{1}{2}LY_A$. Alternatively, the angles $\tan^{-1}X_A$ and $\tan^{-1}Y_A$ could be used as local "Cartesian" coordinates on these cube faces. These angle-based Cartesian coordinates have the advantage of giving a more uniform mapping of the Euclidean plane onto the image of the cube face on the sphere, so they are the preferred choice for numerical work. Global Cartesian coordinates constructed from these angle-based coordinates are defined by

$$x_A^x = c_A^x + \frac{2L}{\pi}\tan^{-1}X_A, \tag{A.5}$$

$$x_A^y = c_A^y + \frac{2L}{\pi}\tan^{-1}Y_A, \tag{A.6}$$

where X_A and Y_A are functions of the standard angular coordinates θ and φ by the expressions given in Table A.4.

For representations of $S^2 \times S^1$, an appropriate coordinate is also needed for the periodically identified z direction in Fig. A.10. Introduce an angle χ, whose range is $-\pi \leqslant \chi \leqslant \pi$, that labels the points in the S^1 subspace. Then define the global Cartesian coordinate associated with this direction as

$$x_A^z = c_A^z + \frac{L}{2\pi}\chi. \tag{A.7}$$

The standard constant-curvature "round" metric on $S^2 \times S^1$ is smooth, and it is therefore an acceptable choice for the reference metric to define the differential structure on this manifold. The simplest representation of this round metric uses the angular coordinates θ, φ, and χ:

$$ds^2 = R_2^2(d\theta^2 + \sin^2\theta d\varphi^2) + R_1^2 d\chi^2, \tag{A.8}$$

where R_2 and R_1 are constants that specify the radii of the S^2 and S^1 parts of the geometry respectively. Using the transformations given in Eqs. (A.5)–(A.7) and Table A.4, a straightforward (but lengthy) calculation gives the global multi-cube Cartesian-coordinate representation of this metric on $S^2 \times S^1$:

$$ds^2 = \left(\frac{\pi R_2}{2L}\right)^2 \frac{(1+X_A^2)(1+Y_A^2)}{(1+X_A^2+Y_A^2)^2}[(1+X_A^2)(dx_A^x)^2 - 2X_AY_Adx_A^xdx_A^y + (1+Y_A^2)(dx_A^y)^2] + \left(\frac{2\pi R_1}{L}\right)^2(dx_A^z)^2. \tag{A.9}$$

The X_A and Y_A that appear in this expression are thought of as the functions of the Cartesian coordinates obtained by inverting the expressions given in Eqs. (A.5) and (A.6):

$$X_A = \tan\left[\frac{\pi(x_A^x - c_A^x)}{2L}\right], \tag{A.10}$$

$$Y_A = \tan\left[\frac{\pi(x_A^y - c_A^y)}{2L}\right]. \tag{A.11}$$

The functions X_A and Y_A depend on the location of a particular coordinate region through the parameters c_A^x and c_A^y. However, beyond this dependence the multi-cube coordinate representation of the $S^2 \times S^1$ round metric given in Eq. (A.9) is the same in each of the six coordinate regions $\mathcal{B}_A$.

These multi-cube Cartesian coordinates $\{x_A, y_A, z_A\}$ turn out to be harmonic with respect to the round metric on $S^2 \times S^1$, i.e. each coordinate is a solution (locally within each cubic-region, not globally across the interface boundaries) to the covariant Laplace equation, $0 = \nabla_A^i\nabla_{Ai}x_A = \nabla_A^i\nabla_{Ai}y_A = \nabla_A^i\nabla_{Ai}z_A$, where ∇_{Ai} is the covariant derivative associated with the $S^2 \times S^1$ metric in region A. These conditions are equivalent to $0 = \partial_{Ai}\left(\sqrt{g_A}g_A^{ij}\right)$ where $g_A = \det g_{Aij}$ and g_A^{ij} is the inverse of the metric g_{Aij} expressed in terms of the multi-cube Cartesian coordinates in region A.

A.3. Multi-cube representation of S^3

The locations of the eight cubic regions used to construct this representation of S^3 are illustrated in Fig. A.11. The values of the cube-center location vectors $\vec{c}_A$ for this configuration are summarized in Table A.6. The inner faces of the touching cubes in Fig. A.11 are assumed to be connected by identity maps. The outer faces of these eight cubic regions are identified using the maps described in Table A.7. This "cubed-sphere" representation of S^3 is a natural three-dimensional generalization of the two-dimensional cubed-sphere representation of S^2 described in Appendix A.2. It is constructed by inserting a four-dimensional cube into a three-dimensional sphere S^3 in R^4, and then identifying points on the faces of the four-cube with the points on the three-sphere that are connected by rays extending outward from the origin.

It is appropriate to discuss this "cubed-sphere" representation of S^3 in some detail, since it does not appear to have been used or described in the literature before. Let $\{\bar{x}, \bar{y}, \bar{z}, \bar{w}\}$ denote Cartesian coordinates in R^4, and let $\bar{x}^2 + \bar{y}^2 + \bar{z}^2 + \bar{w}^2 = r^2$ denote a three-sphere, S^3, of radius r. It is often useful to identify points in S^3 using the angular coordinates χ, θ and φ:

$$\bar{x} = r\sin\chi\sin\theta\cos\varphi, \tag{A.12}$$
$$\bar{y} = r\sin\chi\sin\theta\sin\varphi, \tag{A.13}$$
$$\bar{z} = r\sin\chi\cos\theta, \tag{A.14}$$
$$\bar{w} = r\cos\chi. \tag{A.15}$$

Now consider a four-cube centered at the origin, of size $L = r$ (which just fits inside the three-sphere), whose orientation is aligned with the $\{\bar{x}, \bar{y}, \bar{z}, \bar{w}\}$ axes. Let $\partial_{\bar{z}}\overline{\mathcal{B}}$ denote the eight faces of this four-cube (each of which is a three-cube) labeled by
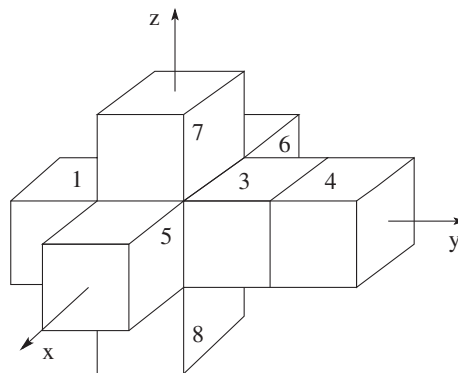
Fig. A.11. The three-manifold S^3 can be represented using the eight cubic regions illustrated here. Cubic region $\mathcal{B}_2$, centered at the origin $\vec{c}_2 = (0, 0, 0)$ is hidden between $\mathcal{B}_7$ and $\mathcal{B}_8$ in this figure. The outer faces of these cubes are identified using the maps described in Table A.7.

Table A.6
Cube-Center Locations for S^3.

$\vec{c}_1 = (0,-L,0)$	$\vec{c}_3 = (0,L,0)$	$\vec{c}_5 = (L,0,0)$	$\vec{c}_7 = (0,0,L)$
$\vec{c}_2 = (0,0,0)$	$\vec{c}_4 = (0,2L,0)$	$\vec{c}_6 = (-L,0,0)$	$\vec{c}_8 = (0,0,-L)$

Table A.7
Cubic Region Face Identifications, $\partial_\alpha \mathcal{B}_A \leftrightarrow \partial_\beta \mathcal{B}_B$, and rotation matrices, $\mathbf{C}_{B\beta}^{A\alpha}$, for the interface maps in S^3.

$\partial_\alpha \mathcal{B}_A \leftrightarrow \partial_\beta \mathcal{B}_B$	$\mathbf{C}_{B\beta}^{A\alpha}$	$\mathbf{C}_{A\alpha}^{B\beta}$	$\partial_\alpha \mathcal{B}_A \leftrightarrow \partial_\beta \mathcal{B}_B$	$\mathbf{C}_{B\beta}^{A\alpha}$	$\mathbf{C}_{A\alpha}^{B\beta}$
$\partial_{+y}\mathcal{B}_1 \leftrightarrow \partial_{-y}\mathcal{B}_2$	$\mathbf{I}$	$\mathbf{I}$	$\partial_{-y}\mathcal{B}_1 \leftrightarrow \partial_{+y}\mathcal{B}_4$	$\mathbf{I}$	$\mathbf{I}$
$\partial_{+x}\mathcal{B}_1 \leftrightarrow \partial_{-y}\mathcal{B}_5$	$\mathbf{R}_{+z}$	$\mathbf{R}_{-z}$	$\partial_{-x}\mathcal{B}_1 \leftrightarrow \partial_{-y}\mathcal{B}_6$	$\mathbf{R}_{-z}$	$\mathbf{R}_{+z}$
$\partial_{+z}\mathcal{B}_1 \leftrightarrow \partial_{-y}\mathcal{B}_7$	$\mathbf{R}_{-x}$	$\mathbf{R}_{+x}$	$\partial_{-z}\mathcal{B}_1 \leftrightarrow \partial_{-y}\mathcal{B}_8$	$\mathbf{R}_{+x}$	$\mathbf{R}_{-x}$
$\partial_{+y}\mathcal{B}_2 \leftrightarrow \partial_{-y}\mathcal{B}_3$	$\mathbf{I}$	$\mathbf{I}$	$\partial_{+x}\mathcal{B}_2 \leftrightarrow \partial_{-x}\mathcal{B}_5$	$\mathbf{I}$	$\mathbf{I}$
$\partial_{-x}\mathcal{B}_2 \leftrightarrow \partial_{+x}\mathcal{B}_6$	$\mathbf{I}$	$\mathbf{I}$	$\partial_{+z}\mathcal{B}_2 \leftrightarrow \partial_{-z}\mathcal{B}_7$	$\mathbf{I}$	$\mathbf{I}$
$\partial_{-z}\mathcal{B}_2 \leftrightarrow \partial_{+z}\mathcal{B}_8$	$\mathbf{I}$	$\mathbf{I}$	$\partial_{+y}\mathcal{B}_3 \leftrightarrow \partial_{-y}\mathcal{B}_4$	$\mathbf{I}$	$\mathbf{I}$
$\partial_{+x}\mathcal{B}_3 \leftrightarrow \partial_{+y}\mathcal{B}_5$	$\mathbf{R}_{-z}$	$\mathbf{R}_{+z}$	$\partial_{-x}\mathcal{B}_3 \leftrightarrow \partial_{+y}\mathcal{B}_6$	$\mathbf{R}_{+z}$	$\mathbf{R}_{-z}$
$\partial_{+z}\mathcal{B}_3 \leftrightarrow \partial_{+y}\mathcal{B}_7$	$\mathbf{R}_{+x}$	$\mathbf{R}_{-x}$	$\partial_{-z}\mathcal{B}_3 \leftrightarrow \partial_{+y}\mathcal{B}_8$	$\mathbf{R}_{-x}$	$\mathbf{R}_{+x}$
$\partial_{+x}\mathcal{B}_4 \leftrightarrow \partial_{+x}\mathcal{B}_5$	$\mathbf{R}_{+z}^2$	$\mathbf{R}_{+z}^2$	$\partial_{-x}\mathcal{B}_4 \leftrightarrow \partial_{-x}\mathcal{B}_6$	$\mathbf{R}_{+z}^2$	$\mathbf{R}_{+z}^2$
$\partial_{+z}\mathcal{B}_4 \leftrightarrow \partial_{+z}\mathcal{B}_7$	$\mathbf{R}_{+x}^2$	$\mathbf{R}_{+x}^2$	$\partial_{-z}\mathcal{B}_4 \leftrightarrow \partial_{-z}\mathcal{B}_8$	$\mathbf{R}_{+x}^2$	$\mathbf{R}_{+x}^2$
$\partial_{+z}\mathcal{B}_5 \leftrightarrow \partial_{+x}\mathcal{B}_7$	$\mathbf{R}_{-y}$	$\mathbf{R}_{+y}$	$\partial_{-z}\mathcal{B}_5 \leftrightarrow \partial_{+x}\mathcal{B}_8$	$\mathbf{R}_{+y}$	$\mathbf{R}_{-y}$
$\partial_{+z}\mathcal{B}_6 \leftrightarrow \partial_{-x}\mathcal{B}_7$	$\mathbf{R}_{+y}$	$\mathbf{R}_{-y}$	$\partial_{-z}\mathcal{B}_6 \leftrightarrow \partial_{-x}\mathcal{B}_8$	$\mathbf{R}_{-y}$	$\mathbf{R}_{+y}$

Table A.8
Cubed-Sphere Representation of S^3.

A	$\bar{\alpha}$	X_A	Y_A	Z_a
1	$-\bar{y}$	$-\frac{\bar{x}}{\bar{y}} = -\cot\varphi$	$-\frac{\bar{w}}{\bar{y}} = -\cot\chi\csc\theta\csc\varphi$	$-\frac{\bar{z}}{\bar{y}} = -\cot\theta\csc\varphi$
2	$+\bar{w}$	$\frac{\bar{x}}{\bar{w}} = \tan\chi\sin\theta\cos\varphi$	$\frac{\bar{y}}{\bar{w}} = \tan\chi\sin\theta\sin\varphi$	$\frac{\bar{z}}{\bar{w}} = \tan\chi\cos\theta$
3	$+\bar{y}$	$\frac{\bar{x}}{\bar{y}} = \cot\varphi$	$-\frac{\bar{w}}{\bar{y}} = -\cot\chi\csc\theta\csc\varphi$	$\frac{\bar{z}}{\bar{y}} = \cot\theta\csc\varphi$
4	$-\bar{w}$	$-\frac{\bar{x}}{\bar{w}} = -\tan\chi\sin\theta\cos\varphi$	$\frac{\bar{y}}{\bar{w}} = \tan\chi\sin\theta\sin\varphi$	$-\frac{\bar{z}}{\bar{w}} = -\tan\chi\cos\theta$
5	$+\bar{x}$	$-\frac{\bar{w}}{\bar{x}} = -\cot\chi\csc\theta\sec\varphi$	$\frac{\bar{y}}{\bar{x}} = \tan\varphi$	$\frac{\bar{z}}{\bar{x}} = \cot\theta\sec\varphi$
6	$-\bar{x}$	$-\frac{\bar{w}}{\bar{x}} = -\cot\chi\csc\theta\sec\varphi$	$-\frac{\bar{y}}{\bar{x}} = -\tan\varphi$	$-\frac{\bar{z}}{\bar{x}} = -\cot\theta\sec\varphi$
7	$+\bar{z}$	$\frac{\bar{x}}{\bar{z}} = \tan\theta\cos\varphi$	$\frac{\bar{y}}{\bar{z}} = \tan\theta\sin\varphi$	$-\frac{\bar{w}}{\bar{z}} = -\cot\chi\sec\theta$
8	$-\bar{z}$	$-\frac{\bar{x}}{\bar{z}} = -\tan\theta\cos\varphi$	$-\frac{\bar{y}}{\bar{z}} = -\tan\theta\sin\varphi$	$-\frac{\bar{w}}{\bar{z}} = -\cot\chi\sec\theta$

the index $\bar{\alpha} = \pm\bar{x}$, etc. Arrange the images of these eight three-cubes in R^3 at the locations given in Table A.6, as shown in Fig. A.11. Table A.8 gives the relationship between the four-cube face identifiers $\bar{\alpha} = \pm\bar{x}$, etc. and the three-cube region identifiers $A = 1, 2, \ldots, 8$ shown in Fig. A.11.

Points on each of the four-cube faces, $\partial_\alpha \overline{\mathcal{B}}$, can be identified by their local Cartesian coordinates. For example, points on the $\bar{\alpha} = +\bar{w}$ face, i.e. the $A = 2$ region in Fig. A.11, can be identified by the coordinates $\{\bar{x}, \bar{y}, \bar{z}\}$. It is convenient to introduce scaled local Cartesian coordinates, $\{X_A, Y_A, Z_A\}$ to represent the points on these faces. For the $\bar{\alpha} = +\bar{w}$ face for example, set $\{X_2, Y_2, Z_2\} = \{\bar{x}/\bar{w}, \bar{y}/\bar{w}, \bar{z}/\bar{w}\}$. Each coordinate has been divided by $\bar{w}$, which is constant on this face, to ensure that the scaled coordinates $\{X_2, Y_2, Z_2\}$ are confined to the ranges, $-1 \leqslant X_2 \leqslant 1$, $-1 \leqslant Y_2 \leqslant 1$, and $-1 \leqslant Z_2 \leqslant 1$. Similar definitions are made on the other faces, cf. Table A.8, that ensure the X_A, Y_A, and Z_A are all oriented the same way as in Fig. A.11, and all satisfy $-1 \leqslant X_A \leqslant 1$, $-1 \leqslant Y_A \leqslant 1$, and $-1 \leqslant Z_A \leqslant 1$. Using Eqs. (A.12)–(A.15), this construction provides a natural identification between points on the original three-sphere, labeled by their angular coordinates $\{\chi, \theta, \varphi\}$, and the local Cartesian coordinates $\{X_A, Y_A, Z_A\}$ on each four-cube face via the equations summarized in Tables A.8 and A.9.

The $\{X_A, Y_A, Z_A\}$ defined using this cubed-sphere construction are local Cartesian coordinates on each of the faces of the four-cube. They could be converted to global coordinates by adding the appropriate offset for each cube: $x_A^x = c_A^x + \frac{1}{2}LX_A$, $x_A^y = c_A^y + \frac{1}{2}LY_A$, and $x_A^z = c_A^z + \frac{1}{2}LZ_A$. Alternatively, the angles $\tan^{-1} X_A$, $\tan^{-1} Y_A$, and $\tan^{-1} Z_A$ also provide local Cartesian-like coordinates for these cubes. These angle-based Cartesian coordinates give a more uniform mapping of Euclidean space onto the image of the four-cube face on the three-sphere. So as in the two-dimensional cubed-sphere case, these angle-based Cartesian coordinates are the preferred choice for numerical work on the multi-cube representation of S^3. Global multi-cube Cartesian coordinates constructed from these angle-based coordinates are defined by

$$x_A^x = c_A^x + \frac{2L}{\pi}\tan^{-1} X_A, \tag{A.16}$$

$$x_A^y = c_A^y + \frac{2L}{\pi}\tan^{-1} Y_A, \tag{A.17}$$

$$x_A^z = c_A^z + \frac{2L}{\pi}\tan^{-1} Z_A, \tag{A.18}$$

Table A.9

Cartesian to Angular Coordinate Map for the Cubed-Sphere Representation of S^3. The range of the local Cartesian coordinate X_A is $-1 \leqslant X_A \leqslant 1$, the range of Z_A is $-1 \leqslant Z_A \leqslant 1$, the range of the angular coordinate θ is $0 \leqslant \theta \leqslant \pi$, and the range of χ is $0 \leqslant \chi \leqslant \pi$ in these expressions. The ranges of φ corresponding to different ranges of Y_A are specified in the table. The quantities $W_A \equiv \sqrt{1 + X_A^2 + Y_A^2 + Z_A^2}$ are used to simplify the expressions for $\cos \chi$.

A	Y_A-range	$\cos \varphi$	φ-range	$\cos \theta$	$\cos \chi$
1	$-1 \leqslant Y_1 \leqslant 1$	$X_1/\sqrt{1 + X_1^2}$	$\frac{7\pi}{4} \geqslant \varphi \geqslant \frac{5\pi}{4}$	$Z_1/\sqrt{1 + X_1^2 + Z_1^2}$	Y_1/W_1
2	$1 \geqslant Y_2 \geqslant 0$	$X_2/\sqrt{X_2^2 + Y_2^2}$	$\pi \geqslant \varphi \geqslant 0$	$Z_2/\sqrt{X_2^2 + Y_2^2 + Z_2^2}$	$1/W_2$
2	$-1 \leqslant Y_2 < 0$	$X_2/\sqrt{X_2^2 + Y_2^2}$	$2\pi > \varphi \geqslant \pi$	$Z_2/\sqrt{X_2^2 + Y_2^2 + Z_2^2}$	$1/W_2$
3	$-1 \leqslant Y_3 \leqslant 1$	$X_3/\sqrt{1 + X_3^2}$	$\frac{3\pi}{4} \geqslant \varphi \geqslant \frac{\pi}{4}$	$Z_3/\sqrt{1 + X_3^2 + Z_3^2}$	$-Y_3/W_3$
4	$1 \geqslant Y_4 > 0$	$X_4/\sqrt{X_4^2 + Y_4^2}$	$2\pi > \varphi \geqslant \pi$	$Z_4/\sqrt{X_4^2 + Y_4^2 + Z_4^2}$	$-1/W_4$
4	$-1 \leqslant Y_4 \leqslant 0$	$X_4/\sqrt{X_4^2 + Y_4^2}$	$\pi \geqslant \varphi \geqslant 0$	$Z_4/\sqrt{X_4^2 + Y_4^2 + Z_4^2}$	$-1/W_4$
5	$-1 \leqslant Y_5 < 0$	$1/\sqrt{1 + Y_5^2}$	$2\pi > \varphi \geqslant \frac{7\pi}{4}$	$Z_5/\sqrt{1 + Y_5^2 + Z_5^2}$	$-X_5/W_5$
5	$1 \geqslant Y_5 \geqslant 0$	$1/\sqrt{1 + Y_5^2}$	$\frac{\pi}{4} \geqslant \varphi \geqslant 0$	$Z_5/\sqrt{1 + Y_5^2 + Z_5^2}$	$-X_5/W_5$
6	$-1 \leqslant Y_6 < 0$	$-1/\sqrt{1 + Y_6^2}$	$\frac{5\pi}{4} \geqslant \varphi > \pi$	$Z_6/\sqrt{1 + Y_6^2 + Z_6^2}$	X_6/W_6
6	$1 \geqslant Y_6 \geqslant 0$	$-1/\sqrt{1 + Y_6^2}$	$\pi \geqslant \varphi \geqslant \frac{3\pi}{4}$	$Z_6/\sqrt{1 + Y_6^2 + Z_6^2}$	X_6/W_6
7	$1 \geqslant Y_7 \geqslant 0$	$X_7/\sqrt{X_7^2 + Y_7^2}$	$\pi \geqslant \varphi \geqslant 0$	$1/\sqrt{1 + X_7^2 + Y_7^2}$	$-Z_7/W_7$
7	$-1 \leqslant Y_7 < 0$	$X_7/\sqrt{X_7^2 + Y_7^2}$	$2\pi > \varphi \geqslant \pi$	$1/\sqrt{1 + X_7^2 + Y_7^2}$	$-Z_7/W_7$
8	$1 \geqslant Y_8 \geqslant 0$	$X_8/\sqrt{X_8^2 + Y_8^2}$	$\pi \geqslant \varphi \geqslant 0$	$-1/\sqrt{1 + X_8^2 + Y_8^2}$	Z_8/W_8
8	$-1 \leqslant Y_8 < 0$	$X_8/\sqrt{X_8^2 + Y_8^2}$	$2\pi > \varphi \geqslant \pi$	$-1/\sqrt{1 + X_8^2 + Y_8^2}$	Z_8/W_8

where X_A, Y_A, and Z_A are functions of the hyper-spherical angular coordinates χ, θ and φ given by the expressions in Tables A.8 and A.9.

The standard constant-curvature "round" metric on S^3 is smooth, and it is therefore an acceptable choice for the reference metric to define the differential structure on this manifold. The simplest representation of this round metric uses the angular coordinates χ, θ, and φ:

$$ds^2 = R_3^2(d\chi^2 + \sin^2 \chi \, d\theta^2 + \sin^2 \chi \sin^2 \theta \, d\varphi^2), \tag{A.19}$$

where R_3 is a constant that specifies the radius of the S^3. Using the transformations given in Eqs. (A.12)–(A.15), and in Tables A.8 and A.9, a straightforward (but lengthy) calculation gives the global multi-cube Cartesian-coordinate representation of this metric on S^3:

$$ds^2 = \left(\frac{\pi R_3}{2L}\right)^2 \frac{(1 + X_A^2)(1 + Y_A^2)(1 + Z_A^2)}{(1 + X_A^2 + Y_A^2 + Z_A^2)^2} \left[\frac{(1 + X_A^2)(1 + Y_A^2 + Z_A^2)}{(1 + Y_A^2)(1 + Z_A^2)} (dx_A^x)^2 - \frac{2X_A Y_A}{1 + Z_A^2} dx_A^x dx_A^y \right.$$
$$\left. + \frac{(1 + Y_A^2)(1 + X_A^2 + Z_A^2)}{(1 + X_A^2)(1 + Z_A^2)} (dx_A^y)^2 - \frac{2X_A Z_A}{1 + Y_A^2} dx_A^x dx_A^z + \frac{(1 + Z_A^2)(1 + X_A^2 + Y_A^2)}{(1 + X_A^2)(1 + Y_A^2)} (dx_A^z)^2 - \frac{2Y_A Z_A}{1 + X_A^2} dx_A^y dx_A^z \right]. \tag{A.20}$$

The X_A, Y_A, and Z_A that appear in Eq. (A.20) are thought of as the functions of the global multi-cube Cartesian coordinates obtained by inverting the expressions given in Eqs. (A.16)–(A.18):

$$X_A = \tan\left[\frac{\pi(x_A^x - c_A^x)}{2L}\right], \tag{A.21}$$

$$Y_A = \tan\left[\frac{\pi(x_A^y - c_A^y)}{2L}\right], \tag{A.22}$$

$$Z_A = \tan\left[\frac{\pi(x_A^z - c_A^z)}{2L}\right]. \tag{A.23}$$

The functions X_A, Y_A and Z_A depend on the location of a particular coordinate region through the parameters c_A^x, c_A^y and c_A^z. However, beyond this dependence the multi-cube coordinate representation of the S^3 round-sphere metric given in Eq. (A.20) is the same in each of the eight coordinate regions $\mathcal{B}_A$.

These multi-cube Cartesian coordinates $\{x_A, y_A, z_A\}$ turn out to be harmonic with respect to the round metric on S^3, i.e. each coordinate is a solution (locally within each cubic-region, not globally across the interface boundaries) to the covariant Laplace equation, $0 = \nabla_A^i \nabla_{Ai} x_A = \nabla_A^i \nabla_{Ai} y_A = \nabla_A^i \nabla_{Ai} z_A$, where ∇_{Ai} is the covariant derivative associated with the S^3 metric in

region A. These conditions are equivalent to $0 = \partial_{Ai}\left(\sqrt{g_A}\,g_A^{ij}\right)$ where $g_A = \det g_{Aij}$ and g_A^{ij} is the inverse of the metric g_{Aij} expressed in terms of the multi-cube Cartesian coordinates in region A.

Appendix B. Spherical harmonics on S^3

This appendix derives expressions for the eigenfunctions of the Laplace operator on the three-sphere S^3. These eigenfunctions are referred to here as three-sphere harmonics. These functions are defined as solutions of the equation

$$\nabla^i \nabla_i Y = -\lambda Y, \tag{B.1}$$

where ∇_i is the covariant derivative operator on S^3, and λ is an eigenvalue. These functions have been studied previously by a number of authors [26–29]. Here a slightly different representation is introduced that allows these harmonics (of arbitrary order) to be evaluated accurately in a straightforward way. Using the angular coordinate representation of the round metric on S^3 from Eq. (A.19), it is straightforward to write the co-variant Laplace operator explicitly as

$$\nabla^i \nabla_i Y = \frac{\partial_\chi[\sin^2 \chi \partial_\chi Y]}{R_3^2 \sin^2 \chi} + \frac{\partial_\theta[\sin \theta \partial_\theta Y]}{R_3^2 \sin \theta \sin^2 \chi} + \frac{\partial_\varphi^2 Y}{R_3^2 \sin^2 \theta \sin^2 \chi}. \tag{B.2}$$

The eigenvalue problem, Eq. (B.1), can be solved then by separation of variables. The non-singular solutions to this equation have the form:

$$Y_{k\ell m}(\chi, \theta, \varphi) = \frac{N_{k\ell m}}{\sqrt{\sin \chi}} Q_{k+\frac{1}{2}}^{\ell+\frac{1}{2}}(\cos \chi) P_\ell^m(\cos \theta) e^{im\varphi}, \tag{B.3}$$

where P_ν^μ and Q_ν^μ are the associated Legendre functions of the first and second kind respectively. The eigenvalue associated with this $Y_{k\ell m}$ is

$$\lambda = \frac{k(k+2)}{R_3^2}. \tag{B.4}$$

These functions are non-singular on S^3 only for integers k, ℓ and m satisfying

$$k \geqslant 0, \tag{B.5}$$
$$k \geqslant \ell \geqslant 0, \tag{B.6}$$
$$\ell \geqslant m \geqslant -\ell. \tag{B.7}$$

The half-integer associated Legendre functions $Q_{k+\frac{1}{2}}^{\ell+\frac{1}{2}}(x)$ with $x = \cos \chi$ are non-singular for $-1 \leqslant x \leqslant 1$, and can be evaluated re-cursively. For fixed ℓ, the functions with $k < \ell$ can be shown to vanish,

$$Q_{k+\frac{1}{2}}^{\ell+\frac{1}{2}}(x) = 0, \tag{B.8}$$

using Section 3.4 Eq. (13) in Ref. [30]. For $k = \ell$ a similar argument using Section 3.6.1 Eq. (14) in Ref. [30] gives

$$Q_{\ell+\frac{1}{2}}^{\ell+\frac{1}{2}}(x) = (-1)^{\ell+1} 2^\ell \ell! \sqrt{\frac{\pi}{2}} (1 - x^2)^{\frac{\ell}{2}+\frac{1}{4}}. \tag{B.9}$$

The functions with $k > \ell$ can be determined from these using the recursion relation,

$$(k - \ell + 2) Q_{k+\frac{5}{2}}^{\ell+\frac{1}{2}}(x) = 2(k+2) x Q_{k+\frac{3}{2}}^{\ell+\frac{1}{2}}(x) - (k + \ell + 2) Q_{k+\frac{1}{2}}^{\ell+\frac{1}{2}}(x), \tag{B.10}$$

from Section 3.8 Eq. (12) in Ref. [30]. Evaluating Eq. (B.10) for $k = \ell - 1$ gives

$$Q_{\ell+\frac{3}{2}}^{\ell+\frac{1}{2}}(x) = 2(\ell+1) x Q_{\ell+\frac{1}{2}}^{\ell+\frac{1}{2}}(x), \tag{B.11}$$

using Eq. (B.8). The $Q_{k+\frac{1}{2}}^{\ell+\frac{1}{2}}(x)$ with $k \geqslant \ell + 2$ can then be generated recursively using Eq. (B.10). This recursion relation is known to be a stable and accurate way to generate the Legendre functions of the first kind, $P_\ell^m(x)$, cf. Ref. [31]. Our numerical tests indicate that it is also an accurate way to generate the half-integer Legendre functions of the second kind, $Q_{k+\frac{1}{2}}^{\ell+\frac{1}{2}}(x)$.

The orthogonality properties of the $Y_{k\ell m}(\chi, \theta, \varphi)$ are determined by the orthogonality properties of $Q_{k+\frac{1}{2}}^{\ell+\frac{1}{2}}(\cos \chi)$, $P_m^\ell(\cos \theta)$ and $e^{im\varphi}$. The needed condition for $Q_{k+\frac{1}{2}}^{\ell+\frac{1}{2}}$ can be obtained from the associated Legendre differential equation,

$$0 = \frac{d}{dx}\left[(1 - x^2) \frac{dQ_\nu^\mu}{dx}\right] + \left[\nu(\nu+1) - \frac{\mu^2}{1-x^2}\right] Q_\nu^\mu, \tag{B.12}$$

from which it follows that

$$\frac{d}{dx}\left[(1 - x^2)\left(Q_{\nu'}^\mu \frac{dQ_\nu^\mu}{dx} - Q_\nu^\mu \frac{dQ_{\nu'}^\mu}{dx}\right)\right] = (\nu' - \nu)(\nu + \nu' + 1) Q_{\nu'}^\mu Q_\nu^\mu. \tag{B.13}$$

The half-integer associated Legendre functions are well behaved in the interval $-1 \leqslant x \leqslant 1$, therefore integrating Eq. (B.13) over this interval gives

$$0 = (v' - v)(v + v' + 1) \int_{-1}^{1} Q_{v'}^{\mu}(x) Q_{v}^{\mu}(x) dx. \tag{B.14}$$

It follows that the $Q_{k+\frac{1}{2}}^{\ell+\frac{1}{2}}(x)$ with $k \geqslant 0$ and $\ell \geqslant 0$ satisfy the orthogonality condition:

$$M_{k\ell}^2 \delta_{k'k} = \int_{-1}^{1} Q_{k'+\frac{1}{2}}^{\ell+\frac{1}{2}}(x) Q_{k+\frac{1}{2}}^{\ell+\frac{1}{2}}(x) dx, \tag{B.15}$$

where $M_{k\ell}$ is the numerical constant,

$$M_{k\ell}^2 = \frac{\pi^2 (k + \ell + 1)!}{4(k + 1)(k - \ell)!}. \tag{B.16}$$

The analogous orthogonality relations for $P_m^{\ell}(\cos \theta)$ and $e^{im\varphi}$ are well known:

$$N_{\ell m}^2 \delta_{\ell' \ell} = \int_{-1}^{1} P_{\ell'}^{m}(y) P_{\ell}^{m}(y) dy, \tag{B.17}$$

$$2\pi \delta_{m'm} = \int_{0}^{2\pi} e^{im'\varphi} e^{-im\varphi} d\varphi, \tag{B.18}$$

where

$$N_{\ell m}^2 = \frac{(\ell + m)!}{(\ell - m)!(\ell + \frac{1}{2})}. \tag{B.19}$$

From these conditions then, it follows that by choosing the normalization constants

$$N_{k\ell m} = \frac{1}{\sqrt{2\pi} M_{k\ell} N_{\ell m}}, \tag{B.20}$$

the $Y_{k\ell m}$ satisfy the following orthogonality conditions on S^3,

$$\begin{aligned}
\int Y_{k'\ell'm'} Y_{k\ell m}^* \sqrt{g} \, d^3x &= R_3^3 \int_0^{\pi} d\chi \int_0^{\pi} d\theta \int_0^{2\pi} d\varphi \, \sin^2 \chi \, \sin \theta \, Y_{k'\ell'm'} Y_{k\ell m}^*, \\
&= \left[\frac{1}{M_{k\ell}^2} \int_{-1}^{1} Q_{k'+\frac{1}{2}}^{\ell'+\frac{1}{2}}(x) Q_{k+\frac{1}{2}}^{\ell+\frac{1}{2}}(x) \, dx \right] \left[\frac{1}{N_{\ell m}^2} \int_{-1}^{1} P_{\ell'}^{m}(y) P_{\ell}^{m}(y) \, dy \right] \left[\frac{1}{2\pi} \int_0^{2\pi} e^{im'\varphi} e^{-im\varphi} d\varphi \right], \\
&= R_3^3 \, \delta_{k'k} \delta_{\ell'\ell} \delta_{m'm}. \tag{B.21}
\end{aligned}$$

References

[1] C. Ronchi, R. Iacono, P.S. Paolucci, The "cubed sphere": a new method for the solution of partial differential equations in spherical geometry, J. Comput. Phys. 124 (1996) 93.
[2] M. Taylor, J. Tribbia, M. Iskandarani, The spectral element method for the shallow water equations on the sphere, J. Comput. Phys. 130 (1997) 92–108.
[3] J.M. Dennis, Partitioning with space-filling curves on the cubed-sphere, in: Proceedings of the 17th International Symposium on Parallel and Distributed Processing, IEEE Computer Society, 2003, p. 269.
[4] J. Thornburg, A multiple-grid-patch evolution scheme for 3-d black hole excision, in: V.G. Gurzadyan, R.T. Jantzen, R. Ruffini (Eds.), The Ninth Marcel Grossmann Meeting: on Recent Developments in Theoretical and Experimental General Relativity, Gravitation, and Relativistic Field Theories, vol. C, World Scientific, Singapore, River Edge, 2000, pp. 1743–1744.
[5] J. Thornburg, A multiple-grid-patch evolution scheme for 3-d black hole excision, Classical Quantum Gravity 21 (2004) 3665–3692.
[6] L. Lehner, O. Reula, M. Tiglio, Multi-block simulations in general relativity: high order discretizations, numerical stability, and applications, Classical Quantum Gravity 22 (2005) 5283–5322.
[7] E. Schnetter, P. Diener, E.N. Dorband, M. Tiglio, A multi-block infrastructure for three-dimensional time-dependent numerical relativity, Classical Quantum Gravity 23 (2006) S553–S578.
[8] E. Pazos, M. Tiglio, M.D. Duez, L.E. Kidder, S.A. Teukolsky, Orbiting binary black hole evolutions with a multipatch high order finite-difference approach, Phys. Rev. D80 (2009) 024027.
[9] D. Pollney, C. Reisswig, E. Schnetter, N. Dorband, P. Diener, High accuracy binary black hole simulations with an extended wave zone, Phys. Rev. D 83 (2009) 044045.
[10] O. Korobkin, E.B. Abdikamalov, E. Schnetter, N. Stergioulas, B. Zink, Stability of general-relativistic accretion disks, Phys. Rev. D 83 (2011) 043007.
[11] T. Radó, Über den Begriff der Riemannsche Fläche, Acta Univ. Szeged 2 (1925) 101–121.
[12] E.E. Moise, Geometric Topology in Dimensions 2 and 3, Springer-Verlag, New York, 1977.
[13] E.E. Moise, Affine structures in 3-manifolds v, Ann. Math. 56 (1952) 96–114.
[14] M. Hamermesh, Group Theory and its Application to Physical Problems, Dover Publications, New York, 1962.
[15] L.E. Kidder, M.A. Scheel, S.A. Teukolsky, E.D. Carlson, G.B. Cook, Black hole evolution by spectral methods, Phys. Rev. D 62 (2000) 084032.
[16] H.P. Pfeiffer, L.E. Kidder, M.A. Scheel, S.A. Teukolsky, A multidomain spectral method for solving elliptic equations, Comput. Phys. Commun. 152 (2003) 253–273.
[17] M.A. Scheel, H.P. Pfeiffer, L. Lindblom, L.E. Kidder, O. Rinne, S.A. Teukolsky, Solving Einstein's equations with dual coordinate frames, Phys. Rev. D 74 (2006) 04006.

[18] M. Scheel, M. Boyle, T. Chu, L. Kidder, K. Matthews, H. Pfeiffer, High-accuracy waveforms for binary black hole inspiral, merger, and ringdown, Phys. Rev. D 79 (2009) 024003.
[19] B. Szilagyi, L. Lindblom, M.A. Scheel, Simulations of binary black hole mergers using spectral methods, Phys. Rev. D 80 (2009) 124010.
[20] W. McLean, Strongly Elliptic Systems and Boundary Integral Equations, Cambridge University Press, 2000.
[21] L.E. Kidder, L. Lindblom, M.A. Scheel, L.T. Buchman, H.P. Pfeiffer, Boundary conditions for the Einstein evolution system, Phys. Rev. D 71 (2005) 064020.
[22] L. Lindblom, M.A. Scheel, L.E. Kidder, R. Owen, O. Rinne, A new generalized harmonic evolution system, Classical Quantum Gravity 23 (2006) S447–S462.
[23] M. Holst, L. Lindblom, R. Owen, H.P. Pfeiffer, M.A. Scheel, L.E. Kidder, Optimal constraint projection for hyperbolic evolution systems, Phys. Rev. D 70 (2004) 084017.
[24] M.A. Scheel, A.L. Erickcek, L.M. Burko, L.E. Kidder, H.P. Pfeiffer, S.A. Teukolsky, 3D simulations of linearized scalar fields in Kerr spacetime, Phys. Rev. D 69 (2004) 104006.
[25] J.R. Dormand, P.J. Prince, A family of embedded Runge–Kutta formulae, J. Comput. Appl. Math. 6 (1980) 19–26.
[26] E.M. Lifshitz, I.M. Khalatnikov, Investigations in relativistic cosmology, Adv. Phys. 12 (1963) 185.
[27] R.T. Jantzen, Tensor harmonics on the 3-sphere, J. Math. Phys. 19 (1978) 163.
[28] V.D. Sandberg, Tensor spherical harmonics on s^2 and s^3 as eigenvalue problems, J. Math. Phys. 19 (1978) 2441.
[29] K. Tomita, Tensor spherical and pseudo-spherical harmonics in four-dimensional spaces, Prog. Theor. Phys. 68 (1982) 310.
[30] A. Erdélyi (Ed.), Higher Transcendental Functions, vol. 1, McGraw-Hill Book Company, 1953.
[31] W.H. Press, S.A. Teukolsky, W.T. Vetterling, B.P. Flannery, Numerical Recipes in FORTRAN, second ed., Cambridge University Press, Cambridge, England, 1992.